



Bauduin, S., Irwin, P. G. J., Lellouch, E., Cottini, V., Moreno, R., Nixon, C. A., ... Flasar, F. M. (2018). Retrieval of H₂O abundance in Titan's stratosphere: A (re)analysis of CIRS/Cassini and PACS/Herschel observations. *Icarus*, 311, 288-305.
<https://doi.org/10.1016/j.icarus.2018.04.003>

Peer reviewed version

License (if available):
CC BY-NC-ND

Link to published version (if available):
[10.1016/j.icarus.2018.04.003](https://doi.org/10.1016/j.icarus.2018.04.003)

[Link to publication record in Explore Bristol Research](#)
PDF-document

This is the author accepted manuscript (AAM). The final published version (version of record) is available online via Elsevier at <https://www.sciencedirect.com/science/article/pii/S0019103517308096> . Please refer to any applicable terms of use of the publisher.

University of Bristol - Explore Bristol Research

General rights

This document is made available in accordance with publisher policies. Please cite only the published version using the reference above. Full terms of use are available:
<http://www.bristol.ac.uk/pure/about/ebr-terms>

1 Retrieval of H₂O abundance in Titan's stratosphere: a
2 (re)analysis of CIRS/Cassini and PACS/Herschel
3 observations^{1*}

4 S. Bauduin^a, P.G.J. Irwin^a, E. Lellouch^b, V. Cottini^c, R. Moreno^b, C.A.
5 Nixon^d, N.A. Teanby^e, T. Ansty^f

6 ^a*Atmospheric, Oceanic and Planetary Physics, University of Oxford, Parks Road, Oxford*
7 *OX1 3PU, UK*

8 ^b*LESIA-Observatoire de Paris, CNRS, Université Paris 06, Université Paris-Diderot, 5*
9 *Place Jules Janssen, 92195 Meudon, France*

10 ^c*Department of Astronomy, University of Maryland at College Park, College Park, MD*
11 *20742, USA*

12 ^d*Planetary Systems Laboratory, NASA Goddard Space Flight Center, Greenbelt, MD*
13 *20771, USA*

14 ^e*School of Earth Sciences, University of Bristol, Wills Memorial Building, Queens Road,*
15 *Bristol BS8 1RJ, UK*

16 ^f*Department of Space Science, Cornell University, Ithaca, NY 14853, USA*

17 **Abstract**

Since its first measurement 20 years ago by the Infrared Space Observatory (ISO), the water (H₂O) mole fraction in Titan's stratosphere remains uncertain due to large differences between the determinations from available measurements. More particularly, the recent measurements made from the Herschel observatory (PACS and HIFI) estimated the H₂O mole fraction to be 0.023 ppb at 12.1 mbar. A mixing ratio of 0.14 ppb at 10.7 mbar was, however, retrieved from nadir spatially-resolved observations of Cassini/CIRS. At the same pressure level (10.7 mbar), this makes a difference of a factor of 5.5 between PACS and CIRS measurements, and this has notably prevented current models from fully constraining the oxygen flux flowing into Titan's atmosphere. In this work, we try to understand the differences between

the H₂O mole fractions estimated from Herschel/PACS and Cassini/CIRS observations. The strategy for this is to 1) analyse recent disc-averaged observations of CIRS to investigate if the observation geometry could explain the previous observed differences, and 2) (re)analyse the three types of observation with the same retrieval scheme to assess if previous differences in retrieval codes/methodology could be responsible for the previous discrepancies. With this analysis, we show that using the same retrieval method better reconcile the previous measurements of these instruments. However, the addition of the disc-averaged CIRS observations, instead of confirming the consistency between the different datasets, reveals discrepancies between one of the CIRS disc-averaged set of observations and PACS measurements. This raises new questions regarding the possibility of latitudinal variations of H₂O, which could be triggered by seasonal changes of the meridional circulation. As it has already been shown for nitriles and hydrocarbons, this circulation could potentially impact the latitudinal distribution of H₂O through the subsidence or upwelling of air rich in H₂O. The possible influence of spatial/time variations of the OH/H₂O input flux in Titan's atmosphere is also discussed. The analysis of more observations will be needed in future work to address the questions arising from this work and to improve the understanding of the sources of H₂O in Titan's atmosphere.

18 *Keywords:* Titan, atmosphere, Atmosphere, composition, Spectroscopy,
19 Infrared observations, Satellite, atmosphere

¹*Herschel is an ESA space observatory with science instruments provided by European-led Principal Investigator consortia and with important participation from NASA.*

20 1. Introduction

21 Since the discovery of carbon dioxide (CO_2) more than 30 years ago
22 (Samuelson et al., 1983), the presence of oxygen compounds has been firmly
23 demonstrated in Titan’s atmosphere. Among these, water vapour (H_2O) is
24 deposited in the high atmosphere by external sources. It was measured for
25 the first time in Titan’s stratosphere around 20 years ago by the Infrared
26 Space Observatory (ISO), using the Short Wavelength Spectrometer (SWS)
27 (Coustenis et al., 1998). The two lines recorded at 227.8 and 254 cm^{-1} by this
28 instrument were effectively modelled using a H_2O profile of 0.4 ppb above
29 some cut-off altitude and were mainly sensitive to H_2O in the pressure range
30 $1\text{--}1 \times 10^{-5}$ mbar. After this first detection, de Kok et al. (2007a) made
31 a first attempt to measure stratospheric H_2O with the Composite Infrared
32 Spectrometer (CIRS) on board the NASA Cassini spacecraft. Due to a poor
33 signal-to-noise ratio (SNR), this first analysis of CIRS spectra was unsuccessful,
34 and only an upper limit of 0.9 ppb was determined, which was consistent
35 with ISO observations. These results were, however, later challenged by mea-
36 surements from the Photodetector Array Camera and Spectrometer (PACS)
37 and the Heterodyne Instrument for the Far-Infrared (HIFI) onboard the Her-
38 schel observatory (Moreno et al., 2012). Using both instruments, Moreno
39 et al. (2012) constrained the vertical profile of H_2O , showing that it increases
40 with height, which is consistent with a high altitude source and low-level sink
41 (condensation and photolysis). They retrieved a H_2O volume mixing ratio
42 (VMR) of 0.023 ppb at 12.1 mbar, which is 20-times lower than the VMR
43 (assumed constant with altitude above the saturation level) determined from
44 ISO. Furthermore, Moreno et al. (2012) reanalysed SWS/ISO spectra and

45 showed that the H₂O abundance inferred from those observations needed a
46 downward revision to 0.06 ppb (uniform profile). Almost at the same time,
47 Cottini et al. (2012) performed a second attempt to measure H₂O from nadir
48 and limb CIRS observations. By averaging a large number of nadir spectra
49 recorded over 4 years, they determined a H₂O VMR of 0.14 ppb at 10.7 mbar.
50 From limb observations, they retrieved 0.13 ppb at 115 km (around 6 mbar)
51 and 0.45 ppb at 230 km (around 0.35 mbar), which confirmed that the H₂O
52 mole fraction increases with height. The retrieved abundance, however, dif-
53 fered by about a factor of 4 from the results of Moreno et al. (2012).

54 These uncertainties on the H₂O mole fraction have prevented photochem-
55 ical models from constraining the flux of OH/H₂O into Titan's atmosphere.
56 As a result, it is currently not determined whether the main source of H₂O
57 comes from micrometeorite ablation (English et al., 1996) or from local
58 sources, such as the cryovolcanic activity on Enceladus (e.g. Hansen et al.,
59 2006; Waite et al., 2006; Hansen et al., 2008, 2011). Using HIFI onboard
60 Herschel, Hartogh et al. (2011) detected the Enceladus H₂O torus and pro-
61 posed that the latter could be the main source of H₂O in Saturn's atmosphere.
62 Based on the OH/H₂O input flux required by the model of Hörst et al. (2008)
63 to reproduce the H₂O abundance retrieved from ISO observations, Hartogh
64 et al. (2011) concluded that the Enceladus influx rates at Titan's atmosphere
65 are too small to explain the observed H₂O abundance. However, with the
66 retrieval of H₂O from Herschel, Moreno et al. (2012) estimated new input
67 fluxes and showed that Enceladus surface activity is a viable source of H₂O
68 in Titan's atmosphere. This was confirmed by the recent model of Dobri-
69 jevic et al. (2014), coupling oxygen, nitrogen and hydrocarbon chemistry,

70 which was able with an Enceladus source to reproduce the H₂O abundance
71 retrieved by either Moreno et al. (2012) or Cottini et al. (2012). Note that if
72 the H₂O abundance retrieved by Cottini et al. (2012) is taken as the reference,
73 Dobrijevic et al. (2014) overestimated the thermospheric H₂O mole fraction
74 when compared with the upper limit estimated by Cui et al. (2009) from the
75 Cassini/INMS (Ion Neutral Mass Spectrometer) data. The OH/H₂O input
76 flux determined is, however, very different depending on the reference cho-
77 sen. More particularly, if the flux is determined using the results of Moreno
78 et al. (2012), both Moreno et al. (2012) and Dobrijevic et al. (2014) could not
79 reproduce H₂O and CO₂ abundances at the same time. They respectively
80 obtained CO₂ mole fractions 10 and 4 times lower than the observed abun-
81 dance (de Kok et al., 2007a). Based on the large difference in the atmospheric
82 lifetimes of CO₂ (several hundred years) and H₂O (around 10 years), Moreno
83 et al. (2012) invoked a variable OH/H₂O input flux over long timescales to
84 explain this difference. This scenario has been explored by the recent model
85 of Lara et al. (2014). They showed, however, that when results of Moreno
86 et al. (2012) are considered, a time-dependent input flux does not solve alone
87 the H₂O/CO₂ problem and the addition of another loss term for H₂O, such
88 as a loss to the haze, is required. Understanding the discrepancies between
89 the H₂O mole fractions measured from Herschel and CIRS is therefore cru-
90 cial to better constrain the existing photochemical models, and to improve
91 the knowledge of the source and chemistry of oxygen compounds in Titan’s
92 atmosphere.

93 In this work, we aim to investigate and understand these previous re-
94 ported differences. For this, we analyse recent disc-averaged observations

95 of Titan (2013-2015) made with the CIRS/Cassini instrument and retrieve
96 new H₂O mole fractions. The use of disc-averaged observations allows an
97 easier comparison with Herschel measurements, which share the same view-
98 ing geometry. In addition to a difference in observation geometry, Moreno
99 et al. (2012) and Cottini et al. (2012) also applied distinct retrieval meth-
100 ods and used different *a priori* information and radiative transfer modelling
101 codes to retrieve H₂O. The goal of this work is also to (re)analyse the CIRS
102 and Herschel datasets with the same retrieval scheme. This will allow us to
103 distinguish if the observed discrepancies are due to modelling/retrieval differ-
104 ences or due to other possible sources. In the case of Herschel, we focus only
105 on PACS observations, which have a very similar vertical sensitivity to H₂O
106 as the CIRS measurements. Among the spectra analysed by Cottini et al.
107 (2012), we only consider the nadir spectrum for the same reasons. These
108 observations are presented in more details in section 2. Sections 3 and 4
109 describe, respectively, the forward modelling settings and the retrieval strat-
110 egy developed to analyse all observations. The results are then discussed in
111 section 5.

112 **2. Instruments and observations**

113 *2.1. CIRS*

114 The CIRS instrument is a Fourier transform spectrometer. It is composed
115 of three separate focal planes (FP1, FP3 and FP4) that measure together
116 spectra in the far- and mid-infrared (IR) (full range: 10–1400 cm⁻¹) with
117 an adjustable apodised resolution between 0.5 and 15.5 cm⁻¹. The FP1
118 covers the far-IR spectral range (10–600 cm⁻¹). It has a circular field-of-view

119 (FOV) of 3.9 mrad diameter, whose half of the integrated response is located
120 within 2.5 mrad. The FP3 and FP4 focal planes consist of collinear arrays
121 of 10 pixels each that record spectra in the mid-IR range (respectively 600–
122 1100 cm^{-1} and 1100–1400 cm^{-1}). The size of each FOV is 0.27×0.27 mrad.
123 More details about the instrument can be found elsewhere (e.g. Flasar et al.,
124 2004; Jennings et al., 2017).

125 In this work, four sets of FP1 observations recorded between February
126 2013 and July 2015 at a spectral resolution of 0.5 cm^{-1} are analysed. They
127 were acquired during four different observations at more than 1.5 million
128 kilometres from Titan (Titan Explorations at Apoapse, TEA), and each set
129 include around 800 disc-averaged spectra. The first observation (rev 182)
130 lasted 20 hours whereas the three next ones (revs 202, 206, 209) lasted around
131 12 hours. The sub-spacecraft latitudes of these observations are -41.43° ,
132 50.73° , 48.58° and -0.02° respectively for sets 182, 202, 206 and 219. Details
133 of these four sets are given in Table 1.

134 Because H_2O lines are very weak in the FP1 range, an averaged spectrum
135 has been calculated for each set of observations to increase the SNR. They are
136 shown in Figure 1 for the 125–260 cm^{-1} spectral range. The associated noise
137 has been evaluated using the same method as Teanby et al. (2006). Briefly,
138 two types of standard error are calculated for each set: 1) the standard
139 deviation on the averaged spectrum, and 2) the standard error related to the
140 noise equivalent spectral radiance (NESR) measured from deep space spectra.
141 The maximum of these standard errors is then taken as the measurement
142 error on the averaged spectrum. This measurement error is similar for the
143 four sets, with the minimum found for the 182 (around 1 $\text{nW cm}^{-2} \text{sr}^{-1} \text{cm}$

144 for the spectral range shown in Figure 1) and the maximum for the 206 and
145 219 sets (around $1.4 \text{ nW cm}^{-2} \text{ sr}^{-1} \text{ cm}$). Noise spikes are however located in
146 different ranges: $140\text{--}150 \text{ cm}^{-1}$ for 182, $152\text{--}164 \text{ cm}^{-1}$ for 202, $212\text{--}227 \text{ cm}^{-1}$
147 for 206, and $240\text{--}265 \text{ cm}^{-1}$ for 219. A spike at 191.25 cm^{-1} is common to all
148 sets.

149 From Figure 1, we can see that H_2O lines are at most barely detected.
150 This is not surprising given the small number of spectra averaged together.
151 For comparison, Cottini et al. (2012) averaged thousands of nadir spectra
152 to achieve a sufficient SNR. Among the four sets analysed here, the SNR
153 seems to vary, with only set 182 showing clear H_2O lines. For this set, the
154 SNR of the H_2O lines is estimated to be around 2 for the lines located above
155 200 cm^{-1} and around 3 for the ones below. The difference observed with the
156 other sets is unlikely to be attributable to measurement error differences, the
157 latter being small. The possibility of latitudinal variations will be discussed
158 in section 5.2.4. Note that in section 5.2.1, we will assess if H_2O lines are
159 present in the sets 202, 206 and 219. Note also that the retrieval scheme,
160 which is described in the following sections, has been developed using set 182
161 only.

162 Finally, the nadir spectrum studied previously by Cottini et al. (2012)
163 is reanalysed. This spectrum is an average of around 7000 spectra acquired
164 between December 2004 and December 2008 in a latitudinal bin of $0\text{--}30^\circ\text{N}$
165 (see Figure 1). More details are given in Cottini et al. (2012). This averaged
166 spectrum will be called “CIRS NA” hereafter.

167 *2.2. PACS/Herschel*

168 PACS is one of the three science instruments onboard the Herschel obser-
169 vatory. It is composed of an imaging photometer, covering the spectral range
170 60–210 μm (47.6–181.8 cm^{-1}) over a FOV of $1.75' \times 3.5'$, and of a grating
171 spectrometer, providing observations in the range 55–210 μm at a spectral
172 resolving power between 1000 and 4000 and over a FOV of $47'' \times 47''$, resolved
173 in 5×5 pixels. More details about the instruments can be found in Poglitsch
174 et al. (2010).

175 In this work, we reanalyse the spectra recorded by the PACS spectrometer
176 that were previously studied by Moreno et al. (2012). These consist of disc-
177 averaged observations of three H_2O lines at 66.43 μm (150.5 cm^{-1}), 75.38 μm
178 (132.7 cm^{-1}) and 108.07 μm (92.5 cm^{-1}), expressed as line/continuum ratios.
179 They were recorded on 22nd June 2010 when the apparent distance between
180 Titan and Saturn was close to the maximum elongation (see Moreno et al.
181 (2012) for more details about the observations and their reduction). In addi-
182 tion to H_2O lines, observations of CH_4 lines acquired by PACS at around the
183 same time are also analysed to retrieve temperature information. These were
184 recorded in the range 102–146 μm using the chopped-nodded PACS range
185 spectroscopy mode with a small chopper throw (see PACS observers' manual
186 2013, [http : //herschel.esac.esa.int/Docs/PACS/pdf/pacs_om.pdf](http://herschel.esac.esa.int/Docs/PACS/pdf/pacs_om.pdf)). In this
187 spectral range, two CH_4 lines have been used in this work, at 106.43 μm
188 (94 cm^{-1}) and 119.63 μm (83.6 cm^{-1}). These CH_4 spectra have been reduced
189 from Level 0 to Level 2 within HIPE 15.0.0 (Herschel Interactive Processing
190 Environment), using the Telescope Normalization pipeline (see PACS Data
191 Reduction Guide 2017 for details, [http : //herschel.esac.esa.int/twiki/pub/Pu](http://herschel.esac.esa.int/twiki/pub/Pu)

192 blic/PacsCalibrationWeb/pacs_spec15.pdf), and the final spectrum has been
193 rebinned close to the Nyquist sampling. Note that spectra (CH₄ lines only)
194 reduced in such a way have units of Janskys (Jy) and have been converted to
195 spectral radiance units of W cm⁻² sr⁻¹ cm. Table 2 summarizes the PACS
196 observations analysed in this work, which are shown in Figure 1.

197 **3. Forward model**

198 *3.1. Reference atmosphere and spectroscopic data*

199 A reference atmosphere has been defined for the analysis of all the ob-
200 servations considered. It is composed of 99 levels distributed between 1457
201 and 1.01×10^{-5} mbar. The far-infrared spectrum of Titan's atmosphere, and
202 more especially the continuum level, is affected by collision-induced absorp-
203 tion (CIA) between pairs of N₂, CH₄ and H₂ molecules. The CIA coefficients
204 have been calculated using the work of Borysow and Frommhold (1986a,b,c,
205 1987), Borysow (1991) and Borysow and Tang (1993). The reference vertical
206 profiles of the 3 gases included are shown in Figure 2.a. The profile of CH₄ has
207 been defined according to Niemann et al. (2010) with a volume mixing ratio
208 of around 5.6% close to the surface and of 1.48% in the stratosphere. For H₂,
209 the mixing ratio has been set at 0.101% at all pressure levels (Niemann et al.,
210 2010). In addition to CIA, the continuum shape is also impacted by aerosol
211 absorption. The assumed haze vertical profile is shown in Figure 2.b and is
212 a simplified version built from previous results (de Kok et al., 2007b, 2010b;
213 Tomasko et al., 2008). The haze relative absorption cross-sections adopted
214 were previously used by Teanby et al. (2013) and derived from the volume
215 absorption coefficients of Anderson and Samuelson (2011). Finally, emission

216 lines of different gases are present in the far-infrared range and are mainly
217 those of CO, HCN, CH₄, H₂O, C₄H₂ and C₂N₂. The spectral ranges used in
218 the different steps of our retrieval scheme have, however, been selected to only
219 include either CH₄ and its isotopologues (CH₃D and ¹³CH₄) or H₂O lines.
220 The vertical profiles of CH₃D and ¹³CH₄ we have considered are shown in
221 Figure 2.a and have been calculated using the isotopic ratios determined by
222 Niemann et al. (2010). The choice of the temperature and the H₂O *a priori*
223 profiles will be discussed in the following sections. Note finally that line data
224 were taken from the HITRAN 2004 database (Rothman et al., 2005) and
225 CH₄ line intensities have been revised according to Wishnow et al. (2007).
226 For CIRS, these have been used to calculate k-tables (Lacis and Oinas, 1991)
227 of gaseous opacities (see Teanby et al. (2013) for details) and line-by-line
228 calculations have been performed for the H₂O retrieval. For PACS, given
229 its high spectral resolution, line-by-line calculations have been preferred to
230 the correlated-k method. To decrease the computation time, pre-calculated
231 tables of monochromatic absorption coefficients (hereafter lbl-tables) have
232 been built using the same pressure/temperature grids as for calculating the
233 k-tables.

234 3.2. *Disc-averaged radiance*

235 To analyse both CIRS FP1 (except the nadir spectrum) and PACS ob-
236 servations, it has been necessary to accurately model the disc-averaged radi-
237 ance. More especially, in the case of CIRS, the inhomogeneous response of
238 the FP1 detector has to be taken into account. It has been shown that the
239 disc-averaged spectrum can be calculated using a weighted sum of spectra
240 simulated for discrete FOV located at increasing offsets from Titan's centre

241 (Teanby and Irwin, 2007; Teanby et al., 2013). In this work, a total of 20
 242 synthetic spectra distributed from the centre of Titan to the top of the at-
 243 mosphere has been used to calculate the expected disc-averaged radiance of
 244 Titan. The weights applied to the sum are calculated as explained in Teanby
 245 et al. (2013). In the case of CIRS observations, these weights are multiplied
 246 by the FP1 spatial sensitivity response determined while Cassini was en route
 247 to Saturn (Flasar et al., 2004).

248 4. Analysis strategy

249 The retrieval of H₂O abundance has been performed using the NEMESIS
 250 software (Irwin et al., 2008). This code includes a forward model which can
 251 be solved either using a line-by-line model or the correlated-k method (Lacis
 252 and Oinas, 1991) according to the spectral resolution of the measurement. A
 253 retrieval method is also implemented and is based on the optimal estimation
 254 formalism (Rodgers, 2000). The idea of this inverse method is to determine
 255 the most probable atmospheric state that is consistent with both the spec-
 256 trum and the knowledge of the atmosphere prior to the measurement. This
 257 is done by minimising a cost function ϕ of the form

$$\phi = \left(\mathbf{y} - \mathbf{F}(\mathbf{x})\right)^T \mathbf{S}_\epsilon^{-1} \left(\mathbf{y} - \mathbf{F}(\mathbf{x})\right) + \left(\mathbf{x} - \mathbf{x}_a\right)^T \mathbf{S}_a^{-1} \left(\mathbf{x} - \mathbf{x}_a\right), \quad (1)$$

258 where \mathbf{y} is the measured spectrum, \mathbf{x} is the atmospheric state vector, \mathbf{x}_a
 259 is the *a priori* state vector, \mathbf{S}_ϵ is the measurement covariance matrix (in-
 260 cluding measurement errors), \mathbf{S}_a is the *a priori* covariance matrix (including
 261 the uncertainties on the *a priori* state), and \mathbf{F} is the forward model. The

262 minimisation is performed using an iterative scheme based on the Levenberg-
263 Marquardt method (see Irwin et al. (2008) for more details). Note that in
264 this work, the *a priori* uncertainties are chosen to avoid unconstrained (ele-
265 ments of \mathbf{S}_a are too large) or over-constrained (elements of \mathbf{S}_a are too small)
266 solutions (Irwin et al., 2008).

267 To analyse CIRS and PACS observations, we have developed a retrieval
268 scheme relying on three successive steps: 1) the retrieval of the tropospheric
269 and stratospheric temperatures, 2) the adjustment of the continuum level in
270 the vicinity of the targeted H₂O lines, and 3) the retrieval of H₂O strato-
271 spheric abundance. Because the stratospheric temperatures and the contin-
272 uum level affect the retrieval of H₂O abundance (see below), their associated
273 uncertainties have been evaluated and then propagated to evaluate the total
274 error on the retrieved H₂O abundance. Each step of the analysis is described
275 in more details in the following sections.

276 *4.1. Step 1: Temperature retrieval*

277 Because it affects the strength of H₂O emission lines along with the H₂O
278 abundance itself, stratospheric temperatures have to be retrieved. As well as
279 affecting the strength of H₂O emission lines, the temperature profile also im-
280 pacts the vertical sensitivity to H₂O. The lower boundary of this sensitivity
281 is indeed determined by the condensation level of H₂O, whose height depends
282 on the assumed temperature profile. Colder temperatures move this level to-
283 wards higher altitudes and inversely. For these two reasons, the temperature
284 profile has to be determined before the H₂O retrieval, and more especially in

285 the pressure range of maximal sensitivity to H₂O. From the H₂O Jacobians²
286 shown in Figure 3 (b,d), this range is found to be between 12 and 1 mbar for
287 both disc-averaged CIRS and PACS observations (Jacobians calculated for
288 the CIRS NA spectrum are similar to those of CIRS disc-averaged observa-
289 tions). The temperature over this range of pressure levels is usually retrieved
290 for CIRS observations using the CH₄ ν_4 band of spatially-resolved observa-
291 tions recorded with the FP4 focal planes (e.g. Achterberg et al., 2008, 2011;
292 Vinatier et al., 2010). If these observations are used to build a disc-averaged
293 temperature profile, they have to sample a sufficiently large range of different
294 latitudes and have to be recorded in a same time interval, close to the time of
295 the FP1 disc-averaged observations. This was found to be difficult to achieve.
296 Therefore, we decided to retrieve the whole temperature profile from the far-
297 IR spectrum only. Pure rotational CH₄ lines along with small parts of the
298 continuum level in their vicinity have been used to retrieve stratospheric and
299 tropospheric temperatures. Although this spectral range is mainly sensitive
300 to tropospheric temperatures (Figure 3.a and 3.c), we can see from Figure 3
301 that the temperature Jacobians calculated for the pure CH₄ rotational lines
302 for both instruments are not null in the 12-1 mbar range, especially close to
303 the level where the Jacobians of H₂O are the largest. CH₄ rotational lines
304 are thus partly sensitive to temperatures in this region and this is what has
305 been exploited in the retrieval. The vertical sensitivity of the temperature
306 retrieval will be discussed in section 5.1. In the case of the CIRS NA spec-
307 trum, the temperature is not disc-averaged but has been retrieved using the

²Derivatives of the calculated top-of-atmosphere radiance with respect to the H₂O abundances at the 99 levels of the reference atmosphere

308 same method. In the next subsections, the retrieval settings are described
309 and the method used to assess the errors on the retrieved temperature profile
310 is presented.

311 4.1.1. Retrieval settings

312 For CIRS FP1 observations, the continuous temperature profile has been
313 retrieved using six CH₄ lines, which have the largest sensitivity to strato-
314 spheric temperature (Figure 5), and including the continuum level in their
315 vicinity (Figure 5). In the case of PACS, fewer lines were available and the
316 temperature has been retrieved from the lines located at 106.43 μm (94 cm^{-1})
317 and 119.63 μm (83.6 cm^{-1}). In both cases, the retrieval range has been cho-
318 sen to not include any other lines than CH₄.

319 Depending on the type of observation, we have considered different *a priori*
320 *ori* temperature profiles taking into account the time and the sub-spacecraft
321 latitude at which they were recorded. For CIRS NA and PACS spectra,
322 the *a priori* temperature profile has been set to the temperature profiles
323 respectively assumed by Cottini et al. (2012) and Moreno et al. (2012). Cot-
324 tini et al. (2012) adopted the temperature profile determined by Anderson
325 and Samuelson (2011) at 15°N. The profile used by Moreno et al. (2012)
326 was a combination of 1) the temperatures measured by the Huygens Atmo-
327 spheric Structure Instrument (HASI) between 0 km and 140 km (Fulchignoni
328 et al., 2005), 2) the disc-averaged temperatures measured from CIRS (140–
329 500 km) by Vinatier et al. (2010), 3) temperatures retrieved from INMS
330 (1000–1500 km) (De La Haye et al., 2007), and 4) a decreasing temperature
331 from 165 K to 155 K between 500 km and 1000 km. For the disc-averaged
332 CIRS observations, the *a priori* temperature profile has been built using

333 retrieved profiles from nadir and limb mid-IR CIRS observations (see Fig-
 334 ure 6) (Teanby et al., 2016). Briefly, temperature has been retrieved at four
 335 pressure levels (5.6, 1 mbar from nadir, 0.1 and 0.01 mbar from limb) and
 336 interpolated in time and space to acquire a more global coverage. The tem-
 337 peratures estimated at the sub-spacecraft latitude and at the time of the
 338 disc-averaged observations have been interpolated onto a finer pressure grid
 339 and have been joined onto the HASI profile (Fulchignoni et al., 2005). The
 340 *a priori* uncertainty has been taken at 1% on the whole profile for all the
 341 observations.

342 The measurement covariance matrix \mathbf{S}_ϵ has been considered diagonal and
 343 includes the measurement noise associated with each observations. For CIRS
 344 observations, the retrieval has been performed using the correlated-k method.
 345 Lbl-tables have been used for PACS spectra. To take into account slight dif-
 346 ferences between these methods and line-by-line calculations, forward mod-
 347 elling errors have been added to the diagonal elements of the \mathbf{S}_ϵ . They have
 348 been estimated from differences between spectra simulated with the different
 349 methods using the reference atmosphere described in section 2.

350 4.1.2. Error analysis

351 When using the optimal estimation method, the assessment of the re-
 352 trieval uncertainties is usually performed using the total error covariance
 353 matrix, $\mathbf{S} = (\mathbf{K}^T \mathbf{S}_\epsilon^{-1} \mathbf{K} + \mathbf{S}_a^{-1})^{-1}$, whose square roots of the diagonal elements
 354 correspond to the standard deviation of each retrieved variable included in
 355 the retrieved state vector \mathbf{x}_{ret} (i.e., temperature at each pressure level). The
 356 use of these errors implies that the elements of the *a priori* covariance ma-
 357 trix are very well known and representative of the real uncertainties on the

358 *a priori* profile, which is not the case here. The retrieval random errors have
359 therefore been evaluated using another method. Here, 35 different temper-
360 ature profiles, covering a large range of temperatures, have been built for
361 each observation. Using these profiles and the reference atmosphere defined
362 in section 3.1, synthetic spectra have been generated and random noise has
363 been added (assuming a normal distribution with a standard deviation equal
364 to the noise associated to the observation). The retrieval procedure described
365 in the previous subsection has then been applied to the 35 spectra and the
366 error has been estimated from the differences between the retrieved and real
367 temperature profiles.

368 The systematic error related to the choice of the CH₄ profile used in the
369 retrieval has not been estimated from the above analysis. As already men-
370 tioned, the CH₄ lines are also sensitive to CH₄ abundance and the latter has
371 been fixed to the profile determined by Niemann et al. (2010). The uncertain-
372 ties on this profile propagate to the retrieved temperature profile and have to
373 be taken into account. To assess the error propagation, we have shifted the
374 CH₄ profile by $\pm 11\%$ (Niemann et al., 2010) and retrieved the temperature
375 profile again. The systematic errors are taken as the temperature differ-
376 ence between the retrieval with and without applying the shift. It is also
377 worth mentioning that the CH₄ profile determined by Niemann et al. (2010)
378 is measured at one specific location and is not necessarily representative of
379 the observations analysed here. More especially, Lellouch et al. (2014) have
380 observed latitudinal variations of CH₄ stratospheric mole fraction and have
381 estimated that the latter can be as low as 0.01 at some latitudes. For the
382 sake of completeness we have also evaluated the difference in the retrieved

383 temperature profile if the true stratospheric CH₄ mole fraction is equal to
384 0.01. These different effects will be discussed in section 5.1. Note finally that
385 there is some error on the intensities of the CH₄ pure rotational lines that
386 we have considered. More especially, there is a 10% reduction of the CH₄
387 line intensities between Wishnow et al. (2007) and the more recent values
388 reported by Boudon et al. (2010). However, we have evaluated that this
389 difference leads to a maximum uncertainty of 0.06 K on the temperature
390 profile. This uncertainty is insignificant compared with the other sources of
391 error described above, and will be therefore neglected in the calculation of
392 the total uncertainty on the retrieved H₂O abundance.

393 *4.2. Step 2: Continuum*

394 *4.2.1. CIRS*

395 The second step of the retrieval scheme consists of properly modelling
396 the continuum level, especially in the vicinity of H₂O lines. Indeed, an
397 under(over)-estimation of this level leads to an over(under)-estimation of the
398 H₂O abundance. This level is mainly affected by tropospheric temperatures,
399 aerosols distribution and absorption, and by the CIA between pairs of N₂,
400 CH₄ and H₂ molecules. The retrieval of the temperature profile described in
401 previous section has partly adjusted this level but we have noticed that dif-
402 ferences remain between the simulated and the observed spectra, especially
403 above 120 cm⁻¹ where most of the targeted H₂O lines are located. To reduce
404 these differences, we have retrieved a continuous profile of aerosols in a first
405 stage. The *a priori* profile considered is shown in Figure 2.b and the related
406 uncertainties have been set to 20%. The retrieval has been performed using
407 the correlated-k method for the spectral ranges 70-100 cm⁻¹ and 130-245

408 cm^{-1} , avoiding emission lines of gases and noise spikes. As for temperature,
409 forward modelling errors have been included in the \mathbf{S}_ϵ matrix.

410 The retrieval of aerosols profile brings a slight improvement to the fit of
411 the continuum level but the latter remains unsatisfactory above 120 cm^{-1} .
412 We have assumed that this was due to uncertainties in the spectral depen-
413 dence of the absorption cross-sections of haze that we have considered. To
414 properly fit the observed continuum, keeping the retrieved aerosol profile,
415 we have smoothly adjusted the spectral variations of the aerosol absorption
416 cross-sections in the range $120\text{--}255 \text{ cm}^{-1}$. Note that apart from variations of
417 haze properties, another possible source for the observed continuum residual
418 is the deficiencies in the modelled CIA (de Kok et al., 2010a), which have
419 not been considered here. However, both aerosols and CIA contribute to the
420 radiance mostly below the emitting level of H_2O and, as long as the con-
421 tinuum level is properly fitted, their values should therefore not impact the
422 H_2O retrieval. Example fits to the CIRS spectra are shown in Figure 5.

423 *4.2.2. PACS/Herschel*

424 Because they are expressed as line/continuum ratios, the analysis per-
425 formed on CIRS spectra does not need to be applied to PACS H_2O ob-
426 servations. These ratios have however to be converted into disc-averaged
427 radiances. For this, a continuum level has been simulated using the reference
428 atmosphere and using the temperature profile retrieved after the first step.
429 The ratios have then been rescaled using the modelled continuum.

430 *4.3. Step 3: H₂O retrieval*

431 *4.3.1. Retrieval settings and a priori choice*

432 The last step of the retrieval scheme consists of determining the strato-
433 spheric H₂O abundance. For CIRS observations, this is done using 5 H₂O
434 lines: 132.75, 170.25, 202.75, 208.5, 254 cm⁻¹ (identified in Figure 1 and
435 Figure 5), using line-by-line calculations. In the case of PACS, only three
436 lines are used (described in Table 2) and the retrieval is performed using
437 lbl-tables.

438 According to the optimal estimation method, the *a priori* H₂O profile
439 should represent the best knowledge of the H₂O abundance prior to the mea-
440 surement. The choice of this profile is important as it will affect directly the
441 H₂O retrieved abundance. This choice is, however, in this case difficult be-
442 cause the uncertainties on the H₂O abundance are large, and their reduction
443 is at the centre of this work. Table 3 and Figure 4 present several profiles
444 that could be used as *a priori*. They are either consistent with previous
445 CIRS observations (Cottini et al., 2012) or with the profile determined from
446 Herschel measurements (Moreno et al., 2012). Because it is impossible to
447 establish which of these is the most representative of the true profile, all
448 of them have been considered as *a priori*. This allows us 1) to assess the
449 effect of the *a priori* profile on the retrieval of H₂O abundance, and 2) to
450 determine if one of them is better suited. Note that we have considered only
451 profiles that differ in values and shape. We have therefore not considered
452 the profiles modelled by Dobrijevic et al. (2014) assuming an external source
453 of CO, which are similar to the “IM1”, “IE1” and “IM2” profiles listed in
454 Table 3. The H₂O profiles simulated by Lara et al. (2014) for the comet

455 impact scenario have not been used because this scenario is very unlikely. To
 456 take into account the condensation of H₂O in the low atmosphere, H₂O has
 457 been set to its saturation vapor pressure³ below the condensation level for
 458 all the *a priori* profiles. A scaling factor, set at 1 as a first guess, is retrieved
 459 for each of them considering 100% of *a priori* uncertainties.

460 4.3.2. Error analysis - CIRS

461 The retrieved H₂O abundance is associated to two types of error: 1) the
 462 error on the abundance itself, and 2) the uncertainty on the height at which
 463 this abundance is located. The first one has been evaluated by propagat-
 464 ing the uncertainties of different parameters, and this has been done for the
 465 retrieval case using the “IM2” H₂O profile as *a priori*. We have first con-
 466 sidered the propagation of the random errors on the retrieved temperature
 467 profile and of the measurement noise. For this, the temperature random
 468 errors are incorporated in the measurement covariance matrix \mathbf{S}_ϵ as follows:

$$\mathbf{S}'_\epsilon = \mathbf{S}_\epsilon + \mathbf{K}_{Tp} \mathbf{S}_{Tp} \mathbf{K}_{Tp}^T, \quad (2)$$

469 where \mathbf{K}_{Tp} are the temperature Jacobians calculated for the H₂O retrieval
 470 range, \mathbf{S}_{Tp} includes the random errors on temperature estimated according
 471 to the method described in subsection 4.1.2. The matrix \mathbf{S}'_ϵ has then been
 472 used in the retrieval of H₂O, and the uncertainties on the latter are calculated
 473 from the matrix \mathbf{S} .

³The saturation vapor pressure (P) has been calculated by assuming an expression of the form $P = \exp\left(a + \frac{b}{T} + cT + dT^2\right)$, where T is the temperature and the coefficients a , b , c , d for H₂O are taken equal to 15.278, -5980.3 K, $8.8294 \times 10^{-3} \text{ K}^{-1}$ and $-1.2169 \times 10^{-5} \text{ K}^{-2}$.

474 We have then evaluated the error on the retrieved H₂O mole fraction com-
475 ing from the uncertainty on the continuum level. For this, we have applied
476 a shift to the continuum, representative of the uncertainty of the latter, and
477 retrieved a new H₂O mole fraction. The uncertainty on the continuum has
478 been estimated as the 1σ significance level (68.3%) of the fit described in
479 section 4.2, which is determined by a $\Delta\chi^2$ that depends on the number of
480 retrieved cross-sections (Press et al., 2007).

481 The last source of errors propagated to the H₂O abundance is the tem-
482 perature systematic errors coming from the choice of the CH₄ profile. It has
483 been evaluated by shifting the stratospheric temperature by the systematic
484 uncertainties estimated in section 4.1.2 following a change of $\pm 11\%$ of the
485 CH₄ profile. The H₂O retrieval is then performed with the new temperature
486 profile. The difference in the H₂O mole fraction retrieved with and without
487 the shift of temperature is taken as the systematic uncertainty on the H₂O
488 abundance. Note that the H₂O retrieval has also been performed using the
489 stratospheric temperatures retrieved using a CH₄ mole fraction of 0.01. The
490 impact of this change on the determined H₂O abundance will be discussed
491 separately from the systematic errors.

492 The total uncertainty is finally calculated considering that the random
493 uncertainties (noise, temperature and continuum) are not fully independent
494 of each other, but are independent of the systematic ones resulting from the
495 uncertainty on the CH₄ profile. The random errors have been thus linearly
496 summed and then added to systematic errors by quadrature.

497 Finally, the height at which H₂O is retrieved is taken as the pressure
498 level at which the Jacobians of H₂O are maximum, which is different for the

499 different assumed H₂O a priori profile listed in Table 3. The full width at
500 half maximum of these functions has been used to define the uncertainty on
501 that level.

502 *4.3.3. Error analysis - PACS*

503 The assessment of the error on the H₂O abundance retrieved from the
504 PACS observations is very similar to the one applied for CIRS observations,
505 apart from the evaluation of the continuum uncertainty. Because PACS spec-
506 tra are scaled by a modelled continuum, the continuum level does not need
507 to be fitted and there is no “retrieval” error on this level. However, the mod-
508 elled continuum is associated with a systematic uncertainty related to the
509 choice of the reference atmosphere, which propagates to the H₂O abundance.
510 To evaluate the propagation of this uncertainty, we have to estimate the er-
511 ror on the modelled continuum, and thus on the parameters affecting this
512 level. For tropospheric temperature, random errors calculated as described
513 in section 4.1.2 are taken into account. For the aerosols distribution and
514 the associated absorption cross-sections, based on the retrieval performed
515 on CIRS spectra, we have estimated that their uncertainties are reasonably
516 around 10% and 20% respectively. A new continuum level has then been
517 modelled by scaling these parameters by their respective uncertainties, and
518 the H₂O abundance has been retrieved from the new radiance spectra com-
519 puted. The H₂O difference obtained between the two modelled continuum is
520 taken as the systematic uncertainty on H₂O due to the continuum.

521 **5. Results**

522 *5.1. Temperature*

523 *5.1.1. CIRS disc-averaged*

524 Figure 6 (a-d) shows the *a priori* and retrieved temperature profiles for
525 the four CIRS disc-averaged observations. For all of them, the retrieved
526 profile departs from the *a priori* by about 1.5 K in the troposphere (at
527 pressure levels larger than 100 mbar) and by up to 4 K in the stratosphere
528 (between 100 and 1 mbar) for the 182, 202, 206 observations, and by up to
529 7 K for the set 219. Figure 5 shows the fit to the set 182 as an example.
530 The vertical sensitivity of the temperature retrieval can be discussed using
531 the associated averaging kernel (AVK) functions (Figure 6 (e-h)). The AVK
532 functions represent the sensitivity of the retrieved state \mathbf{x}_{ret} to the true state
533 \mathbf{x}_{tr} (Rodgers, 2000). The height at which they reach their largest value
534 provides an estimation of the height of the retrieval maximum sensitivity.
535 The AVK are included in a matrix (\mathbf{A}) calculated according to:

$$\mathbf{A} = \frac{\partial \mathbf{x}_{\text{ret}}}{\partial \mathbf{x}_{\text{tr}}} = (\mathbf{K}^T \mathbf{S}_\epsilon^{-1} \mathbf{K} + \mathbf{S}_a^{-1})^{-1} \mathbf{K}^T \mathbf{S}_\epsilon^{-1} \mathbf{K}, \quad (3)$$

536 where \mathbf{K} is the Jacobian matrix of the retrieval. From Figure 6 (e-h), we
537 can see that for the four disc-averaged observations the maximum sensitivity
538 to temperature is found between 400 and 200 mbar as it was expected from
539 the Jacobians (Figure 3.a). The temperature sensitivity stays large up to
540 70 mbar and then starts to decrease as moving upwards in the atmosphere. In
541 the pressure range of sensitivity to H₂O, the AVK functions still present non
542 zero values and show that the retrieval is also partly sensitive to temperatures

543 in this region. At pressure levels lower than 1 mbar, where CH₄ lines are not
544 sensitive to temperature (from Jacobians and AVK), the retrieved profile
545 stays close to the *a priori* profile.

546 The random retrieval error on the temperature profile is shown in Fig-
547 ure 7.a, and has been calculated for the set 182. Given the very similar noise
548 levels and retrieval diagnostics (AVK, DOFS,...), we can reasonably assume
549 that the error will be of the same order of magnitude for the four sets. It
550 decreases from 1 K at the surface to about 0.3 K around 100 mbar, where
551 the maximal sensitivity to temperature is found. It increases then to 0.4 K
552 and stays constant up to 7 mbar, where it starts to increase again to 1 K at
553 1 mbar. From this level, as the sensitivity of CH₄ lines to temperature de-
554 creases, it increases and reaches more than 2 K. The systematic errors on the
555 retrieved temperature profile are shown in Figure 7.b in absolute value for
556 the set 182. We can see that the choice of CH₄ stratospheric abundance has a
557 significant impact on the retrieved temperatures. This is especially the case
558 in the range of sensitivity to H₂O, where the differences reach around 2 K
559 when the CH₄ profile is shifted by $\pm 11\%$ (mole fraction of CH₄ equals 1.32%
560 and 1.64%). In the case where the CH₄ mole fraction is reduced to 0.01, these
561 differences are even larger and reach more than 5 K in the 12-1 mbar range.
562 Note that in this case the retrieved temperature profile is warmer than the
563 *a priori* profile. The impact of the assumed CH₄ profile is of the same or-
564 der of magnitude for the three other sets. The impact of these temperature
565 differences on the H₂O retrieval will be assessed in subsection 5.2.1.

566 5.1.2. CIRS nadir

567 Figure 8.a shows the temperature profile retrieved from the CIRS NA
568 spectrum and the fit is shown in Figure 5. In the troposphere, it is very
569 similar to the *a priori* profile and this was expected since tropospheric tem-
570 peratures were retrieved by Cottini et al. (2012) using CH₄ pure rotational
571 lines. However, in the 12-1 mbar region, the retrieved profile is significantly
572 different from the profile used by Cottini et al. (2012), which was taken from
573 Anderson and Samuelson (2011) and was not retrieved from the analyzed
574 spectrum. The differences are up to 8 K. Such temperature difference very
575 likely impacts the retrieval of the stratospheric H₂O abundance and this will
576 be investigated in subsection 5.2.2.

577 As seen from the AVK functions shown in Figure 8.b, the vertical sen-
578 sitivity of the retrieval is very similar to the one observed for disc-averaged
579 CIRS spectra. The AVK functions reach their maximum values between 400
580 and 200 mbar, where the sensitivity to temperature is maximal. Their values
581 then start to decrease, but the retrieval still show sensitivity to temperature
582 in the pressure range of maximum sensitivity to H₂O.

583 The random uncertainties on the temperature profile are shown in Fig-
584 ure 8.c. They are well below 1 K in the troposphere, especially in the range
585 400-30 mbar, where the sensitivity to temperature is maximal. In the re-
586 gion of sensitivity to H₂O, these errors are within 0.9-1.6 K, which is slightly
587 larger than the ones estimated for disc-averaged observations. As already
588 noticed in the previous subsection, the CH₄ profile has a large influence on
589 the retrieved profile in the range 12-1 mbar (Figure 8.d). The systematic
590 errors are estimated at around 2 K in absolute value if we consider $\pm 11\%$

591 of uncertainty on the CH₄ profile. If the stratospheric CH₄ mole fraction is
592 reduced to 0.01, the retrieved temperature profile is warmer by up to 8 K
593 than the one shown in Figure 8.a.

594 5.1.3. PACS

595 Figure 9 presents the temperature profile retrieved from PACS observa-
596 tions along with the associated error and vertical sensitivity diagnostics. As
597 observed for the CIRS NA case, the retrieved profile is significantly colder, by
598 up to 9 K, from the temperature profile considered by Moreno et al. (2012)
599 in the range of H₂O sensitivity. As a reminder, Moreno et al. (2012) did not
600 determine the temperature profile from PACS spectra but built one based
601 on several retrievals performed in different studies. The observed difference
602 could possibly lead to the retrieval of a larger H₂O abundance, and then
603 therefore to a better agreement between CIRS and Herschel measurements.
604 This will be discussed in more details in subsection 5.2.3. The fit to the
605 spectrum is shown in Figure 5.

606 From the AVK functions shown in Figure 9.b, we can see that the retrieval
607 has less vertical resolution than those performed on CIRS observations. The
608 maximum sensitivity to temperature is found to be within 200 and 70 mbar
609 and thus show lower sensitivity to temperature in the lower troposphere.
610 This was expected from the temperature Jacobians (Figure 3.c) and explains
611 that the retrieved profile stays close to the *a priori* in the low atmosphere.
612 As observed for CIRS observations, the retrieval, however, show sensitivity
613 to temperature in the pressure range of maximum sensitivity to H₂O. The
614 smaller vertical resolution likely explains the larger random errors on the
615 profile in the 12-1 mbar range, which reach more than 4 K (Figure 9.c).

616 Systematic errors (absolute value) are within 2-3 K in the same range when
617 the uncertainty on CH₄ profile is assumed to be ±11%. If the stratospheric
618 CH₄ mole fraction is reduced to 0.01, the retrieved temperature profile is
619 warmer by up to 9 K. The propagation of these uncertainties to the H₂O
620 abundance will be discussed in section 5.2.3.

621 5.2. H₂O abundance

622 Table 4 shows a summary of the H₂O retrievals performed on the different
623 observations analysed in this work. For comparison, the H₂O abundances re-
624 trieved when the stratospheric temperatures are determined assuming 1.00%
625 of stratospheric CH₄ are also indicated. Note that they are calculated for the
626 pressure range indicated. Example fits are shown in Figure 5. The following
627 subsections discuss first of all the retrieval for each type of observation and
628 then compare the retrieved H₂O abundances.

629 5.2.1. CIRS disc-averaged

630 5.2.1.1 CIRS 182

631 From Table 4, considering all the different *a priori* H₂O profiles, we can see
632 that the H₂O VMR retrieved from the set 182 is found to be within 0.120 ppb
633 and 0.215 ppb in the 8.2–5.1 mbar pressure range. This shows that the choice
634 of the *a priori* profile has a significant impact on the retrieved H₂O abun-
635 dance. The total column of H₂O above the condensation level is, however,
636 less affected by the H₂O vertical profile assumptions and is determined to
637 be within $3.5\text{--}3.8\times 10^{14}$ molecules/cm². Because the *a priori* profiles have
638 different slopes (Figure 4), they have also an effect on the height of maxi-
639 mum sensitivity to H₂O, which varies from 8.2 mbar to 5.1 mbar. For all

640 retrievals, the fits are reasonably good with associated χ^2 around 1.48–1.49.
641 Given these very similar values, it is therefore impossible to determine which
642 *a priori* profile is the most appropriate, and all of them are kept in the fol-
643 lowing discussions. The total error has been estimated at -43%/+44%. The
644 largest contribution to the total error is the uncertainty on the continuum
645 level, which is estimated at $\pm 27\%$. Finally, when the stratospheric temper-
646 atures retrieved using a CH_4 mole fraction of 0.01 are considered, the H_2O
647 VMRs are around 40% smaller and fall within 0.072–0.131 ppb.

648 5.2.1.2 Other sets

649 Compared to the set 182, the three other disc-averaged spectra do not show
650 clear H_2O lines as can be seen in Figure 1. Before performing the retrieval, we
651 have first of all assessed if the presence of H_2O lines is statistically attested.
652 To do this, we have calculated the misfit χ^2 as a function of the scaling factor
653 (MF) applied to the H_2O profile (the “IM2” *a priori* profile is considered),
654 starting at MF=0. If H_2O emission lines are present in the spectrum, the χ^2
655 function should show a minimum at the best fitting scaling factor. Because
656 we are adjusting one parameter (the scaling factor), a 3σ detection requires
657 a χ^2 decrease of 9 compared to the case assuming no H_2O . Figure 10 shows
658 the $\Delta\chi^2(\chi^2 - \chi^2(\text{MF} = 0))$ functions calculated for each sets. For all of
659 them, the minimum is found below the limit $\Delta\chi^2 = -9$, meaning that H_2O
660 is detected at the 3σ level. The minimum χ^2 is found at MF=0.75 for the
661 set 202, and at MF=0.55 for the sets 206 and 219.

662 As the presence of H_2O emission lines has been statistically confirmed,
663 we have applied the retrieval scheme to the three sets in a second stage. The

664 results are summarized in Table 4. The retrieved scaling factors are very
665 close to those determined from the χ^2 analysis: they are equal to 0.76, 0.58
666 and 0.59 respectively for the sets 202, 206 and 219. These correspond to
667 respective H₂O VMRs of 0.129 ppb, 0.099 ppb, and 0.100 ppb at 5.6 mbar.
668 As seen for the set 182, the choice of the *a priori* H₂O profile has a strong
669 influence, leading to retrieved VMRs varying within 0.080–0.151 ppb for the
670 set 202, 0.059–0.119 ppb for the set 206, and 0.054–0.120 ppb for the set
671 219, mainly between 8 mbar and 5 mbar. The total columns of H₂O are
672 more stable against the choice of the *a priori* H₂O profile and are found
673 to be within $2.3\text{--}2.6\times 10^{14}$ molecules/cm², $1.7\text{--}2.0\times 10^{14}$ molecules/cm², 1.6--
674 2.1×10^{14} molecules/cm² respectively for sets 202, 206, and 219. The assess-
675 ment of the most appropriate *a priori* is impossible for the three sets because
676 all profiles lead to very similar quality of fit. The reduced χ^2 values are found
677 to be 1.65–1.66, 1.40 and 1.20–1.21 respectively for sets 202, 206 and 219.
678 The estimated total errors are larger than those assessed for the set 182. This
679 was expected given the smaller SNR of the averaged spectra for the three
680 other sets. These errors are equal to -56%/+57%, $\pm 65\%$, and -70%/+78%
681 respectively for sets 202, 206 and 219. Finally, as seen for set 182, when us-
682 ing the stratospheric temperature profile determined for a stratospheric CH₄
683 mole fraction of 0.01, the retrieved H₂O VMRs are smaller. They fall within
684 0.038–0.081 ppb, 0.038–0.082 ppb and 0.032–0.075 ppb respectively for sets
685 202, 206 and 219.

686 5.2.2. CIRS nadir

687 Using the scheme developed for disc-averaged CIRS spectra, the H₂O
688 VMR retrieved from the CIRS NA spectrum falls within 0.058 ppb–0.109 ppb

689 in the 9.6–5.4 mbar pressure range. This VMR is smaller by a factor 1.3–
690 2.4 than the one determined by Cottini et al. (2012) (0.14 ppb) and this
691 shows the influence of the chosen retrieval scheme on the evaluation of the
692 H₂O abundance. This difference is mostly associated with the choice of the
693 *a priori* profile. Indeed, by redoing the retrieval using a constant H₂O *a*
694 *priori* profile of 0.1 ppb above the saturation level as Cottini et al. (2012),
695 we retrieve a H₂O VMR of 0.138 ppb, which is in very good agreement with
696 the value reported by Cottini et al. (2012). However, because the H₂O mole
697 fraction has been firmly demonstrated to increase with height, a H₂O profile
698 constant at all altitudes is not the best option for the *a priori* profile and
699 was therefore not considered in this work. Note that if the total errors are
700 taken into account (-42%/+44% for this work, ±0.05 ppb for Cottini et al.
701 (2012)), the largest H₂O abundances determined in this work agree within
702 the error bars with the results of Cottini et al. (2012). Note finally that the
703 discrepancies mentioned above are even larger when the H₂O abundance is
704 retrieved using the stratospheric temperatures determined for a stratospheric
705 CH₄ mole fraction of 0.01. The retrieved H₂O VMRs are in this case a factor
706 of 1.7–3.2 smaller than the one reported by Cottini et al. (2012).

707 As we already mentioned, the assumed temperature profile affects the
708 height of the H₂O condensation level and therefore the vertical sensitivity
709 to H₂O. Because the temperature profile we retrieved is colder than the one
710 assumed by Cottini et al. (2012), the maximum sensitivity to H₂O is found
711 to be higher in the atmosphere (9.6–5.4 mbar) than determined by Cottini
712 et al. (2012) (maximum sensitivity at 10.7 mbar). Note also that, as seen for
713 CIRS disc-averaged observations, determining the most appropriate H₂O *a*

714 *a priori* profile is impossible based on the χ^2 values (0.67–0.68 for the reduced
715 χ^2).

716 5.2.3. PACS

717 Before applying the retrieval scheme described in section 4 to the PACS
718 observations, we have determined if differences in retrieval codes might have
719 a significant impact on the H₂O abundance. For this, we first retrieved H₂O
720 using very similar retrieval assumptions as those used by Moreno et al.
721 (2012), i.e., using the same temperature profile and considering the “Sa”
722 profile as *a priori* (Table 3 and Figure 4). With these settings, we retrieve a
723 scaling factor of 0.96 to be applied to the “Sa” profile, which is in excellent
724 agreement with the results of Moreno et al. (2012). To investigate the effect
725 of the choice of the *a priori* profile, we then performed the retrievals using
726 the different profiles shown in Table 3. The retrieved H₂O abundances vary
727 between 0.015–0.031 ppb, and fall well within the error bars estimated by
728 Moreno et al. (2012).

729 Since differences in retrieval codes do not affect the retrieved H₂O abun-
730 dance, we have investigated in a second stage if differences in the retrieval
731 method, especially differences in the temperature profile, significantly affect
732 the retrieved H₂O abundance from PACS. For this, we have applied the anal-
733 ysis described in section 4 and the results are shown in Table 4. The retrieved
734 VMRs are found to be within 0.024–0.052 ppb and are slightly larger than
735 those determined by Moreno et al. (2012). This shows the impact of the
736 temperature profile retrieved from PACS CH₄ lines, which was found to be
737 colder than the one assumed by Moreno et al. (2012). This temperature pro-
738 file also explains that the H₂O maximum sensitivity is found higher in the

739 atmosphere (8.2–5.6 mbar) because the condensation level moves upwards.
740 The H₂O VMRs retrieved when considering the stratospheric temperature
741 profile determined using 1.00% for the stratospheric CH₄ mole fraction are,
742 however, in good agreement with those determined by Moreno et al. (2012).
743 This is explained by the fact that this temperature profile is very similar to
744 the one considered by Moreno et al. (2012). In this case, the retrieved H₂O
745 VMRs fall within 0.020–0.030 ppb.

746 As already observed for the other types of observations, the H₂O total
747 column is more stable against the choice of the *a priori* H₂O profile and
748 is determined to be within $0.8\text{--}0.9 \times 10^{14}$ molecules/cm². The total errors
749 are estimated to be -15%/+12%. These errors are significantly smaller than
750 those estimated for CIRS. This can be explained by the better SNR of PACS
751 observations. Note that the reduced χ^2 values are very similar for all the *a*
752 *priori* profiles and are within 1.49–1.51.

753 5.2.4. Comparison and discussion

754 Figure 11 compares the H₂O VMRs retrieved for all observations using
755 the same analysis scheme as a function of the H₂O *a priori* profile considered.
756 We can see that the comparison changes slightly depending on the chosen *a*
757 *priori*, which directly impacts the retrieved abundance. The lowest VMRs
758 are retrieved using the “Sa” profile of Moreno et al. (2012) (0.029–0.120 ppb),
759 and the largest using the “L3” profile of Lara et al. (2014) (0.052–0.215 ppb).
760 Because it affects the H₂O retrieved abundance, the choice of the *a priori*
761 profile seems to impact the relative agreement between the different obser-
762 vations. Indeed, the best agreement is found for the “Sa” profile, whereas
763 the retrieved VMRs show larger discrepancies in case of “L1”, “L2”, and

764 “L3” profiles. Note that in the case of the H₂O total column abundance,
765 there is much less impact of the *a priori* profile on the relative agreement
766 between the different datasets. However, despite the differences due to the
767 choice of the H₂O *a priori* profile and whether the total column abundances
768 or the volume mixing ratios are considered, the same general trend is ob-
769 served. For each case, the smallest H₂O abundance is retrieved from PACS
770 spectra confirming the initial discrepancy between Moreno et al. (2012) and
771 Cottini et al. (2012). The CIRS disc-averaged set 182 is associated with the
772 largest H₂O abundance, and a very good agreement is found between the
773 three other disc-averaged sets and the CIRS NA observations. Note that the
774 *a priori* profile also impacts the height of maximum sensitivity (Table 4).
775 For each a priori, when taking into account the FWHM of the Jacobians
776 (not shown), PACS and CIRS seem to sound a very similar pressure region,
777 and the small differences do not explain the variation of the retrieved H₂O
778 VMRs between the different observations.

779 By analysing PACS observations with the same assumptions than Moreno
780 et al. (2012) but with the NEMESIS retrieval code, we have shown that
781 differences in the retrieval codes used by Moreno et al. (2012) and Cottini
782 et al. (2012) hardly explain the differences observed previously between CIRS
783 and PACS measurements. Applying the same retrieval method and making
784 the same H₂O *a priori* assumptions for both PACS and CIRS observations
785 has, on the contrary, decreased the discrepancies observed previously be-
786 tween these instruments (Moreno et al., 2012; Cottini et al., 2012). However,
787 the analysis of the CIRS disc-averaged dataset has brought new differences.
788 Whereas the sets 202, 206, and 219 are in good agreement with the CIRS

789 NA observation and consistent within the error bars with PACS measure-
790 ments, the H₂O VMRs retrieved from the set 182 are significantly larger
791 and especially differ from PACS measurements. This is confirmed by Fig-
792 ure 12, which shows a comparison between observed PACS H₂O lines and
793 lines simulated using the H₂O profiles retrieved for the different observations
794 considering the “Sa” *a priori* profile. Indeed, we can see that the profile
795 retrieved for set 182 strongly overestimates PACS H₂O lines. Also from Fig-
796 ure 12 we can see that, although a relative agreement is found within the
797 error bars between the other CIRS and PACS measurements, the H₂O pro-
798 files retrieved from CIRS observations are inconsistent with PACS H₂O lines.
799 This confirms that H₂O is less abundant for PACS observations. Based on
800 this, the hypothesis of natural variations of the H₂O abundance, triggered
801 by the global circulation in Titan’s atmosphere, can be envisaged. Similarly
802 to nitriles and some hydrocarbons, H₂O shows an increasing mole fraction
803 with height, resulting from a source at high altitudes (either micrometeorite
804 ablation or Enceladus) and a sink in the low atmosphere (condensation and
805 photolysis). The meridional circulation could thus possibly affect the lati-
806 tudinal distribution of H₂O abundance. This has been observed for nitriles
807 and hydrocarbons, for which subsidence of air rich in these gases leads to
808 an enrichment in the stratosphere, and inversely upwelling leads to the de-
809 pletion of their stratospheric abundance (e.g. Coustenis et al., 2007, 2016;
810 Teanby et al., 2006, 2008, 2009, 2010). The observations analysed in this
811 work are recorded at different sub-spacecraft latitudes and at different pe-
812 riods in Titan’s year (see Figure 11), and are therefore subject to different
813 meridional circulation. The CIRS disc-averaged set 182 is recorded in the

814 late southern autumn-early southern winter, when according to dynamical
815 models (e.g. Hourdin et al., 2004) the meridional circulation is dominated
816 by a single Hadley cell with subsidence at the South Pole (Teanby et al.,
817 2012) and upwelling at the North Pole. The sub-spacecraft latitude of this
818 set is -41° but because of its disc-averaged nature, the observation includes
819 the South Pole. It is therefore sensitive to the possible H_2O enhancement
820 brought by the subsidence of air rich in H_2O occurring at the South Pole,
821 and this could explain the larger stratospheric VMRs retrieved for this set
822 (see also Coustenis et al. (2016)). On the contrary, PACS observations were
823 recorded close to the northern spring equinox, for which dynamical models
824 predict a transitional circulation state, in which two cells develop with up-
825 welling at the equator and subsidence at both poles (Hourdin et al., 2004;
826 Vinatier et al., 2015). The PACS sub-spacecraft latitude is close to the equa-
827 tor, where upwelling could cause H_2O depletion and explain the low H_2O
828 abundance retrieved from PACS spectra. Note that the variations of H_2O
829 could be very similar to those observed for C_2H_2 , which has a comparable
830 lifetime of around 10 years. Another origin that could contribute to explain
831 the H_2O VMRs differences is the spatial/time variation of the input $\text{OH}/\text{H}_2\text{O}$
832 flux in Titan's atmosphere. Depending on its source, H_2O is likely deposited
833 at different locations (heights but also latitudes) in Titan's atmosphere. The
834 idea of time variations on scales of decades/centuries has already been put
835 forward by Moreno et al. (2012) to explain the difference of the input flux
836 needed to explain current H_2O and CO_2 abundances. Time variations of
837 the H_2O source rate at Enceladus, although previously debated, have been
838 reported by some recent studies (Hedman et al., 2013; Nimmo et al., 2014;

839 Teolis et al., 2017, e.g.). These variations occur on timescales of a few months
840 or years, which is smaller than the H₂O lifetime, and unlikely explain the H₂O
841 differences observed in this work. Variations on longer timescales cannot be
842 ruled out, but do not provide a complete satisfactory explanation for the
843 differences observed in this work. Indeed, if such variations existed, the H₂O
844 abundance would react over periods of around 10 years. The variations of the
845 H₂O abundance reported in this work occur, however, on shorter timescales.
846 Moreover, assuming that a change of the OH/H₂O flux is responsible for
847 the difference between the H₂O mole fractions retrieved from PACS and the
848 set 182 of CIRS, the good agreement observed between the CIRS NA mea-
849 surement and the three other CIRS disc-averaged sets becomes then more
850 difficult to understand. For this reason, the meridional circulation and its
851 seasonal variations seem at this stage to provide the most reasonable expla-
852 nation for the H₂O abundance differences observed in this work. Note also
853 that longitudinal variations of H₂O are barely possible given the lifetime of
854 H₂O and the strong stratospheric zonal winds that rapidly homogenize gas
855 abundances. Finally, following the work of Coustenis et al. (1998), Moreno
856 et al. (2012) reanalysed SWS/ISO observations and determined a H₂O VMR
857 of 0.06 ppb. Most of the H₂O VMRs determined in this work are in good
858 agreement with this reanalysis.

859 The hypotheses discussed above are hardly proved with the results of this
860 work, given the very few analysed measurements and the large errors asso-
861 ciated with the CIRS observations. The analysis of more observations will
862 be needed in future work to better understand the observed H₂O variations.
863 We also believe that the development of 2D-3D photochemical models, cou-

864 pling Titan’s oxygen chemistry and general circulation, could help address
865 the new issues highlighted in this work. Note that if H₂O is retrieved using
866 stratospheric temperatures determined for a stratospheric CH₄ mole fraction
867 of 0.01, the H₂O VMRs evaluated for the set 182 and for PACS observations
868 remain significantly different, and thus the above discussion still holds. It is
869 worth, however, assessing if this discussion still holds when the CH₄ latitudi-
870 nal variability is taken into account. Indeed, we have considered a constant
871 stratospheric CH₄ mole fraction for all the observations (either 1.48% or
872 1.00%). Based on Lellouch et al. (2014), 1.48% seems to be a relatively good
873 assumption for the CIRS disc-averaged set 182. On the contrary, a mole
874 fraction of 1.00% is best suited for the set 219, the CIRS NA observation
875 and for PACS data. If these CH₄ mole fractions are assumed for these ob-
876 servations, the difference in the retrieved H₂O VMRs between set 182 and
877 the three other observations is larger than when considering constant CH₄
878 abundance, and this strengthens the idea of latitudinal variations of the H₂O
879 abundance. Regarding the sets 202 and 206, it is more difficult to assess what
880 CH₄ mole fraction is the most appropriate, given the large error bars reported
881 by Lellouch et al. (2014). If it is assumed to be in between the extreme values
882 considered in this work, significant differences in the retrieved H₂O VMRs
883 should remain. In future work, attempts to reduce the uncertainty on the
884 stratospheric CH₄ mole fraction, but also on other parameters such as the
885 continuum level, should be undertaken to reduce the total uncertainty on the
886 retrieved H₂O abundance.

887 6. Conclusions

888 The goal of this work was to understand the differences in H₂O abun-
889 dances retrieved previously by Moreno et al. (2012) from Herschel disc-
890 averaged observations, and by Cottini et al. (2012) from the average of a
891 large number of spectra recorded in a 0–30° latitudinal bin. The strategy
892 for this was to 1) analyse disc-averaged observations of CIRS to investigate
893 if the observation geometry could explain the differences, and 2) (re)analyse
894 the three types of observation with the same retrieval scheme to assess if dif-
895 ferences in retrieval codes/methodology could be responsible for the previous
896 discrepancies. For this purpose, four sets of CIRS disc-averaged observations
897 taken between 2013–2015 were analysed. A retrieval scheme composed of
898 three successive steps was also set up. It comprises the retrieval of the tem-
899 perature profile (step 1), the adjustment of the continuum level in the vicinity
900 of H₂O lines (step 2), and the retrieval of the H₂O abundance (step 3). A
901 rigorous error assessment was performed and included the propagation of
902 the uncertainties of key parameters: measurement noise, temperature, CH₄
903 profile (for temperature retrieval), and continuum level. Different H₂O *a pri-*
904 *ori* profiles, either consistent with PACS or CIRS measurements, have been
905 considered for the H₂O retrieval from all observations.

906 With this analysis, we have first of all shown that differences in the re-
907 trieval codes used by Moreno et al. (2012) and Cottini et al. (2012) do not
908 explain the discrepancies observed previously between PACS and CIRS mea-
909 surements. Applying the same retrieval method, including the temperature
910 retrieval, and making the same H₂O *a priori* assumptions for both PACS and
911 CIRS has, on the contrary, better reconciled the measurements of these in-

912 struments, with the agreement depending on the chosen *a priori* H₂O profile.
913 The retrieved H₂O abundances are also in good agreement with the reanal-
914 ysis of ISO observations performed by Moreno et al. (2012). The addition of
915 the disc-averaged CIRS observations, instead of confirming the consistency
916 between the different datasets, has revealed discrepancies mainly between the
917 set 182 and PACS observations. This makes us question the idea that the
918 datasets should be in agreement. The instruments measured H₂O at differ-
919 ent sub-observer latitudes and at different periods in Titan’s year which are
920 associated with different meridional circulation. This circulation is shown to
921 affect the latitudinal distribution of nitriles and hydrocarbons, through the
922 subsidence or upwelling of air rich in these gases. As discussed in this work,
923 the meridional circulation could potentially impact the latitudinal distribu-
924 tion of H₂O as well and explain the differences between the CIRS set 182
925 and PACS measurements. On the contrary, time variations of the OH/H₂O
926 input flux in Titan’s atmosphere, which were shown to occur on timescales
927 of a few months or years by recent studies, unlikely explain the observed
928 differences given the H₂O lifetime of around 10 years. Given the few H₂O
929 measurements and the large uncertainties associated with the CIRS observa-
930 tions, these hypotheses are, however, impossible to evaluate with the results
931 obtained so far.

932 To validate these assumptions, the analysis of more observations will be
933 required in future work. More especially, the NASA Cassini mission covers
934 now almost the half of a Titan year. CIRS FP1 observations of Titan recorded
935 between 2004 and 2017 could be used to determine if the H₂O abundance
936 varies with time and/or latitude. The photochemical models describing the

937 oxygen chemistry in Titan's atmosphere developed until now are 1D models,
938 considering only the vertical transport of gases. In the future 2D-3D mod-
939 els, coupling the oxygen chemistry with the general circulation, should be
940 developed to address the questions arising from this work. Finally, efforts
941 should be undertaken to decrease the uncertainties on the retrieved H₂O
942 abundances, which are revealed to be large for CIRS observations. Reducing
943 the uncertainty of the stratospheric CH₄ mole fraction or on the continuum
944 level, which were shown to significantly affects the H₂O retrieval, should be
945 a priority of any future study.

946 **Acknowledgements**

947 S. Bauduin would like to thank the Wiener-Anspach Foundation (Bel-
948 gium) for her postdoctoral fellowship. N. Teanby is funded by UK Science
949 Technology and Facilities Council. The authors would like to thank the
950 Cassini and CIRS teams involved in building and testing the instrument,
951 planning data acquisition sequences and calibration of the data. PACS has
952 been developed by a consortium of institutes led by MPE (Germany) and in-
953 cluding UVIE (Austria); KU Leuven, CSL, IMEC (Belgium); CEA, LAM
954 (France); MPIA (Germany); INAF-IFSI/OAA/OAP/OAT, LENS, SISSA
955 (Italy); IAC (Spain). This development has been supported by the funding
956 agencies BMVIT (Austria), ESA-PRODEX (Belgium), CEA/CNES (France),
957 DLR (Germany), ASI/INAF (Italy), and CICYT/MCYT (Spain). HCSS /
958 HSpot / HIPE is a joint development (are joint developments) by the Her-
959 schel Science Ground Segment Consortium, consisting of ESA, the NASA
960 Herschel Science Center, and the HIFI, PACS and SPIRE consortia.

961 **References**

962 Achterberg, R. K., Conrath, B. J., Gierasch, P. J., Flasar, F. M., Nixon,
963 C. A., 2008. Titan’s middle-atmospheric temperatures and dynamics ob-
964 served by the Cassini Composite Infrared Spectrometer. *Icarus* 194 (1),
965 263 – 277.

966 Achterberg, R. K., Gierasch, P. J., Conrath, B. J., Flasar, F. M., Nixon,
967 C. A., 2011. Temporal variations of Titans middle-atmospheric tempera-
968 tures from 2004 to 2009 observed by Cassini/CIRS. *Icarus* 211 (1), 686 –
969 698.

970 Anderson, C. M., Samuelson, R. E., 2011. Titans aerosol and stratospheric
971 ice opacities between 18 and 500m: Vertical and spectral characteristics
972 from Cassini CIRS. *Icarus* 212 (2), 762 – 778.

973 Borysow, A., 1991. Modeling of collision-induced infrared absorption spectra
974 of H₂-H₂ pairs in the fundamental band at temperatures from 20 to 300
975 K. *Icarus* 92 (2), 273 – 279.

976 Borysow, A., Frommhold, L., 1986a. Collision-induced rototranslational ab-
977 sorption spectra of N₂-N₂ pairs for temperatures from 50 to 300 K. *The*
978 *Astrophysical Journal* 311, 1043–1057.

979 Borysow, A., Frommhold, L., 1986b. Theoretical collision-induced rototrans-
980 lational absorption spectra for modeling Titan’s atmosphere: H₂-N₂ pairs.
981 *The Astrophysical Journal* 303, 495–510.

- 982 Borysow, A., Frommhold, L., 1986c. Theoretical collision-induced rototrans-
983 lational absorption spectra for the outer planets: H₂-CH₄ pairs. The As-
984 trophysical Journal 304, 849–865.
- 985 Borysow, A., Frommhold, L., 1987. Collision-induced rototranslational ab-
986 sorption spectra of CH₄-CH₄ pairs at temperatures from 50 to 300 K. The
987 Astrophysical Journal 318, 940–943.
- 988 Borysow, A., Tang, C., 1993. Far Infrared CIA Spectra of N₂-CH₄ Pairs for
989 Modeling of Titan’s Atmosphere. Icarus 105 (1), 175 – 183.
- 990 Boudon, V., Pirali, O., Roy, P., Brubach, J.-B., Manceron, L., Auwera, J. V.,
991 2010. The high-resolution far-infrared spectrum of methane at the SOLEIL
992 synchrotron. Journal of Quantitative Spectroscopy and Radiative Transfer
993 111 (9), 1117 – 1129, special Issue Dedicated to Laurence S. Rothman on
994 the Occasion of his 70th Birthday.
- 995 Cottini, V., Nixon, C., Jennings, D., Anderson, C., Gorius, N., Bjoraker,
996 G., Coustenis, A., Teanby, N., Achterberg, R., Bézard, B., de Kok, R.,
997 Lellouch, E., Irwin, P., Flasar, F., Bampasidis, G., 2012. Water vapor in
998 Titans stratosphere from Cassini CIRS far-infrared spectra. Icarus 220 (2),
999 855 – 862.
- 1000 Coustenis, A., Achterberg, R. K., Conrath, B. J., Jennings, D. E., Marten,
1001 A., Gautier, D., Nixon, C. A., Flasar, F. M., Teanby, N. A., Bzard, B.,
1002 Samuelson, R. E., Carlson, R. C., Lellouch, E., Bjoraker, G. L., Romani,
1003 P. N., Taylor, F. W., Irwin, P. G., Fouchet, T., Hubert, A., Orton, G. S.,
1004 Kunde, V. G., Vinatier, S., Mondellini, J., Abbas, M. M., Courtin, R.,

- 1005 2007. The composition of Titan's stratosphere from Cassini/CIRS mid-
1006 infrared spectra. *Icarus* 189 (1), 35 – 62.
- 1007 Coustenis, A., Jennings, D. E., Achterberg, R. K., Bampasidis, G., Lavvas,
1008 P., Nixon, C. A., Teanby, N. A., Anderson, C. M., Cottini, V., Flasar,
1009 F. M., 2016. Titans temporal evolution in stratospheric trace gases near
1010 the poles. *Icarus* 270, 409 – 420.
- 1011 Coustenis, A., Salama, A., Lellouch, E., Encrenaz, T., Bjoraker, G., Samuel-
1012 son, R., de Graauw, T., Feuchtgruber, H., Kessler, M., 1998. Evidence
1013 for water vapor in Titan's atmosphere from ISO/SWS data. *Astronomy*
1014 *Astrophysics* 336, L85–L89.
- 1015 Cui, J., Yelle, R., Vuitton, V., Waite, J., Kasprzak, W., Gell, D., Nie-
1016 mann, H., Mller-Wodarg, I., Borggren, N., Fletcher, G., Patrick, E., Raaen,
1017 E., Magee, B., 2009. Analysis of Titan's neutral upper atmosphere from
1018 Cassini Ion Neutral Mass Spectrometer measurements. *Icarus* 200 (2), 581
1019 – 615.
- 1020 de Kok, R., Irwin, P., Teanby, N., 2010a. Far-infrared opacity sources in
1021 Titans troposphere reconsidered. *Icarus* 209 (2), 854 – 857.
- 1022 de Kok, R., Irwin, P., Teanby, N., Lellouch, E., Bzard, B., Vinatier, S.,
1023 Nixon, C., Fletcher, L., Howett, C., Calcutt, S., Bowles, N., Flasar, F.,
1024 Taylor, F., 2007a. Oxygen compounds in Titan's stratosphere as observed
1025 by Cassini CIRS. *Icarus* 186 (2), 354 – 363.
- 1026 de Kok, R., Irwin, P., Teanby, N., Nixon, C., Jennings, D., Fletcher, L.,
1027 Howett, C., Calcutt, S., Bowles, N., Flasar, F., Taylor, F., 2007b. Char-

1028 characteristics of Titan's stratospheric aerosols and condensate clouds from
1029 Cassini CIRS far-infrared spectra. *Icarus* 191 (1), 223 – 235.

1030 de Kok, R., Irwin, P., Teanby, N., Vinatier, S., Tosi, F., Negrao, A., Osprey,
1031 S., Adriani, A., Moriconi, M., Coradini, A., 2010b. A tropical haze band
1032 in Titans stratosphere. *Icarus* 207 (1), 485 – 490.

1033 De La Haye, V., Waite, J. H., Johnson, R. E., Yelle, R. V., Cravens, T. E.,
1034 Luhmann, J. G., Kasprzak, W. T., Gell, D. A., Magee, B., Leblanc,
1035 F., Michael, M., Jurac, S., Robertson, I. P., 2007. Cassini Ion and Neu-
1036 tral Mass Spectrometer data in Titan's upper atmosphere and exosphere:
1037 Observation of a suprathreshold corona. *Journal of Geophysical Research:*
1038 *Space Physics* 112 (A7), A07309.

1039 Dobrijevic, M., Hébrard, E., Loison, J., Hickson, K., 2014. Coupling of oxy-
1040 gen, nitrogen, and hydrocarbon species in the photochemistry of Titan's
1041 atmosphere. *Icarus* 228, 324 – 346.

1042 English, M., Lara, L., Lorenz, R., Ratcliff, P., Rodrigo, R., 1996. Ablation
1043 and chemistry of meteoric materials in the atmosphere of Titan. *Advances*
1044 *in Space Research* 17 (12), 157 – 160.

1045 Flasar, F. M., Kunde, V. G., Abbas, M. M., Achterberg, R. K., Ade, P.,
1046 Barucci, A., Bézard, B., Bjoraker, G. L., Brasunas, J. C., Calcutt, S.,
1047 et al., 2004. Exploring the Saturn System in the Thermal Infrared: The
1048 Composite Infrared Spectrometer. *Space Science Review* 115, 169–297.

1049 Fulchignoni, M., Ferri, F., Angrilli, F., Ball, A., et al., 2005. In situ mea-

- 1050 surements of the physical characteristics of Titan’s environment. *Nature*
1051 438 (7069), 785–91.
- 1052 Hansen, C., Esposito, L., Stewart, A., Meinke, B., Wallis, B., Colwell, J.,
1053 Hendrix, A., Larsen, K., Pryor, W., Tian, F., 2008. Water vapour jets
1054 inside the plume of gas leaving enceladus. *Nature* 456 (27), 477–479.
- 1055 Hansen, C. J., Esposito, L., Stewart, A. I. F., Colwell, J., Hendrix, A., Pryor,
1056 W., Shemansky, D., West, R., 2006. Enceladus’ Water Vapor Plume. *Sci-*
1057 *ence* 311 (5766), 1422–1425.
- 1058 Hansen, C. J., Shemansky, D. E., Esposito, L. W., Stewart, A. I. F., Lewis,
1059 B. R., Colwell, J. E., Hendrix, A. R., West, R. A., Waite, J. H., Teolis,
1060 B., Magee, B. A., 2011. The composition and structure of the Enceladus
1061 plume. *Geophysical Research Letters* 38 (11), L11202.
- 1062 Hartogh, P., Lellouch, E., Moreno, R., Bockelée-Morvan, D., Biver, N., Cas-
1063 sidy, T., Rengel, M., Jarchow, C., Cavali, T., Crovisier, J., Helmich, F.,
1064 Kidger, M., 2011. Direct detection of the Enceladus water torus with Her-
1065 schel. *A&A* 532, L2.
- 1066 Hedman, M. M., Gosmeyer, C. M., Nicholson, P. D., Sotin, C., Brown, R. H.,
1067 Clark, R. N., Baines, K. H., Buratti, B. J., Showalter, M. R., 2013. An ob-
1068 served correlation between plume activity and tidal stresses on Enceladus.
1069 *Nature* 500 (7461), 182–184.
- 1070 Hörst, S. M., Vuitton, V., Yelle, R. V., 2008. Origin of oxygen species in
1071 Titan’s atmosphere. *Journal of Geophysical Research: Planets* 113 (E10),
1072 E10006.

- 1073 Hourdin, F., Lebonnois, S., Luz, D., Rannou, P., 2004. Titan’s stratospheric
1074 composition driven by condensation and dynamics. *Journal of Geophysical*
1075 *Research: Planets* 109 (E12), E12005.
- 1076 Irwin, P., Teanby, N., de Kok, R., Fletcher, L., Howett, C., Tsang, C., Wil-
1077 son, C., Calcutt, S., Nixon, C., Parrish, P., 2008. The NEMESIS planetary
1078 atmosphere radiative transfer and retrieval tool. *Journal of Quantitative*
1079 *Spectroscopy and Radiative Transfer* 109 (6), 1136 – 1150.
- 1080 Jennings, D. E., Flasar, F. M., Kunde, V. G., Nixon, C. A., Segura, M. E.,
1081 Romani, P. N., Gorius, N., Albright, S., Brasunas, J. C., Carlson, R. C.,
1082 Mamoutkine, A. A., Guandique, E., Kaelberer, M. S., Aslam, S., Achter-
1083 berg, R. K., Bjoraker, G. L., Anderson, C. M., Cottini, V., Pearl, J. C.,
1084 Smith, M. D., Hesman, B. E., Barney, R. D., Calcutt, S., Vellacott, T. J.,
1085 Spilker, L. J., Edgington, S. G., Brooks, S. M., Ade, P., Schinder, P. J.,
1086 Coustenis, A., Courtin, R., Michel, G., Fettig, R., Pilorz, S., Ferrari, C.,
1087 Jun 2017. Composite infrared spectrometer (cirs) on Cassini. *Appl. Opt.*
1088 56 (18), 5274–5294.
- 1089 Lacis, A. A., Oinas, V., 1991. A description of the correlated k distribution
1090 method for modeling nongray gaseous absorption, thermal emission, and
1091 multiple scattering in vertically inhomogeneous atmospheres. *Journal of*
1092 *Geophysical Research: Atmospheres* 96 (D5), 9027–9063.
- 1093 Lara, L., Lellouch, E., González, M., Moreno, R., Rengel, M., 2014. A time-
1094 dependent photochemical model for Titan’s atmosphere and the origin of
1095 H₂O. *A&A* 566, A143.

- 1096 Lellouch, E., Bézard, B., Flasar, F., Vinatier, S., Achterberg, R., Nixon, C.,
1097 Bjoraker, G., Gorius, N., 2014. The distribution of methane in Titan's
1098 stratosphere from Cassini/CIRS observations. *Icarus* 231, 323 – 337.
- 1099 Moreno, R., Lellouch, E., Lara, L. M., Feuchtgruber, H., Rengel, M., Har-
1100 togh, P., Courtin, R., 2012. The abundance, vertical distribution and origin
1101 of H₂O in Titan's atmosphere: Herschel observations and photochemical
1102 modelling. *Icarus* 221 (2), 753 – 767.
- 1103 Niemann, H. B., Atreya, S. K., Demick, J. E., Gautier, D., Haberman, J. A.,
1104 Harpold, D. N., Kasprzak, W. T., Lunine, J. I., Owen, T. C., Raulin,
1105 F., 2010. Composition of Titan's lower atmosphere and simple surface
1106 volatiles as measured by the Cassini-Huygens probe gas chromatograph
1107 mass spectrometer experiment. *Journal of Geophysical Research: Planets*
1108 115 (E12).
- 1109 Nimmo, F., Porco, C., Mitchell, C., 2014. Tidally Modulated Eruptions on
1110 Enceladus: Cassini ISS Observations and Models. *The Astronomical Jour-*
1111 *nal* 148 (3), 46.
- 1112 Poglitsch, A., Waelkens, C., Geis, N., Feuchtgruber, H., Vandenbussche, B.,
1113 Rodriguez, L., Krause, O., Renotte, E., van Hoof, C., Saraceno, P., et al.,
1114 2010. The Photodetector Array Camera and Spectrometer (PACS) on the-
1115 Herschel Space Observatory. *A&A* 518, L2.
- 1116 Press, W. H., Teukolsky, S. A., Vetterling, W. T., Flannery, B. P., 2007. Nu-
1117 merical Recipes: The Art of Scientific Computing, 3rd Edition. Cambridge
1118 University Press.

- 1119 Rodgers, C., 2000. Inverse methods for atmospheric sounding: theory and
1120 practice. World Scientific.
- 1121 Rothman, L., Jacquemart, D., Barbe, A., Benner, D. C., Birk, M., Brown,
1122 L., Carleer, M., Chackerian, C., Chance, K., Coudert, L., Dana, V., Devi,
1123 V., Flaud, J.-M., Gamache, R., Goldman, A., Hartmann, J.-M., Jucks,
1124 K., Maki, A., Mandin, J.-Y., Massie, S., Orphal, J., Perrin, A., Rins-
1125 land, C., Smith, M., Tennyson, J., Tolchenov, R., Toth, R., Auwera,
1126 J. V., Varanasi, P., Wagner, G., 2005. The HITRAN 2004 molecular spec-
1127 troscopic database. *Journal of Quantitative Spectroscopy and Radiative*
1128 *Transfer* 96 (2), 139 – 204.
- 1129 Samuelson, R. E., Maguire, W. C., Hanel, R. A., Kunde, V. G., Jennings,
1130 D. E., Yung, Y. L., Aikin, A. C., 1983. CO₂ on Titan. *Journal of Geophys-*
1131 *ical Research: Space Physics* 88 (A11), 8709–8715.
- 1132 Teanby, N., Irwin, P., de Kok, R., Nixon, C., 2009. Dynamical implications of
1133 seasonal and spatial variations in Titan’s stratospheric composition. *Philo-*
1134 *sophical Transactions of the Royal Society of London A: Mathematical,*
1135 *Physical and Engineering Sciences* 367 (1889), 697–711.
- 1136 Teanby, N., Irwin, P., de Kok, R., Nixon, C., Coustenis, A., Bézard, B., Cal-
1137 cutt, S., Bowles, N., Flasar, F., Fletcher, L., Howett, C., Taylor, F., 2006.
1138 Latitudinal variations of HCN, HC₃N, and C₂N₂ in Titan’s stratosphere
1139 derived from Cassini CIRS data. *Icarus* 181 (1), 243 – 255.
- 1140 Teanby, N., Irwin, P., de Kok, R., Nixon, C., Coustenis, A., Royer, E., Cal-
1141 cutt, S., Bowles, N., Fletcher, L., Howett, C., Taylor, F., 2008. Global and

- 1142 temporal variations in hydrocarbons and nitriles in Titan's stratosphere
1143 for northern winter observed by Cassini/CIRS. *Icarus* 193 (2), 595 – 611.
- 1144 Teanby, N., Irwin, P., Nixon, C., Courtin, R., Swinyard, B., Moreno, R.,
1145 Lellouch, E., Rengel, M., Hartogh, P., 2013. Constraints on Titan's mid-
1146 dle atmosphere ammonia abundance from Herschel/SPIRE sub-millimetre
1147 spectra. *Planetary and Space Science* 75, 136 – 147.
- 1148 Teanby, N., Irwin, P., Nixon, C., de Kok, R., Vinatier, S., Coustenis, A.,
1149 Sefton-Nash, E., Calcutt, S., Flasar, F., 2012. Active upper-atmosphere
1150 chemistry and dynamics from polar circulation reversal on Titan. *Nature*
1151 491, 732–735.
- 1152 Teanby, N. A., Irwin, P., 2007. Quantifying the effect of finite field-of-view
1153 size on radiative transfer calculations of Titan's limb spectra measured by
1154 Cassini-CIRS. *Astrophysics and Space Science* 310 (3-4), 293–305.
- 1155 Teanby, N. A., Irwin, P. G. J., de Kok, R., Nixon, C. A., 2010. Seasonal
1156 Changes in Titan's Polar Trace Gas Abundance Observed by Cassini. *The*
1157 *Astrophysical Journal Letters* 724 (1), L84.
- 1158 Teanby, N. A., Vinatier, S., Sylvestre, M., de Kok, R., Nixon, C., Irwin,
1159 P., 2016. Titan's south polar stratospheric vortex evolution. In: *DPS48*,
1160 509.08.
- 1161 Teolis, B. D., Perry, M. E., Hansen, C. J., Waite, J. H., Porco, C. C., Spencer,
1162 J. R., Howett, C. J. A., 2017. Enceladus Plume Structure and Time Vari-
1163 ability: Comparison of Cassini Observations. *Astrobiology* 17 (9), 926–940.

- 1164 Tomasko, M., Doose, L., Engel, S., Dafoe, L., West, R., Lemmon, M.,
1165 Karkoschka, E., See, C., 2008. A model of Titan's aerosols based on
1166 measurements made inside the atmosphere. *Planetary and Space Science*
1167 56 (5), 669 – 707.
- 1168 Vinatier, S., Bézard, B., Lebonnois, S., Teanby, N. A., Achterberg, R. K.,
1169 Gorius, N., Mamoutkine, A., Guandique, E., Jolly, A., Jennings, D. E.,
1170 Flasar, F. M., 2015. Seasonal variations in Titan's middle atmosphere dur-
1171 ing the northern spring derived from Cassini/CIRS observations. *Icarus*
1172 250, 95 – 115.
- 1173 Vinatier, S., Bézard, B., Nixon, C. A., Mamoutkine, A., Carlson, R. C.,
1174 Jennings, D. E., Guandique, E. A., Teanby, N. A., Bjoraker, G. L., Flasar,
1175 F. M., Kunde, V. G., 2010. Analysis of Cassini/CIRS limb spectra of Titan
1176 acquired during the nominal mission. *Icarus* 205 (2), 559 – 570.
- 1177 Waite, J. H., Combi, M. R., Ip, W.-H., Cravens, T. E., McNutt, R. L.,
1178 Kasprzak, W., Yelle, R., Luhmann, J., Niemann, H., Gell, D., Magee,
1179 B., Fletcher, G., Lunine, J., Tseng, W.-L., 2006. Cassini Ion and Neutral
1180 Mass Spectrometer: Enceladus Plume Composition and Structure. *Science*
1181 311 (5766), 1419–1422.
- 1182 Wishnow, E., Orton, G., Ozier, I., Gush, H., 2007. The distortion dipole
1183 rotational spectrum of CH₄: A low temperature far-infrared study. *Journal*
1184 *of Quantitative Spectroscopy and Radiative Transfer* 103 (1), 102 – 117.

Table 1: Sets of CIRS FP1 disc-averaged observations analysed in this work. The start and end times are in UTC and Titan radius is the projected angular radius of the solid surface. The sub-spacecraft latitudes and Titan radius are the average of each sequence. TEA stands for Titan Explorations at Apoapse.

TEA	Start date	End date	No. spectra	Sub-spacecraft latitude	Titan radius (mrad)
182-001	21/02/2013 8:31:38	22/02/2013 04:21:23	712	-41.43°	1.64
202-001	02/03/2014 22:47:21	03/03/2014 11:56:10	898	50.73°	1.69
206-001	10/07/2014 00:50:30	10/07/2014 12:29:06	793	48.58°	1.67
219-001	23/07/2015 13:57:21	24/07/2015 01:35:55	792	-0.02°	1.63

Table 2: PACS observations of CH₄ and H₂O (see also Moreno et al. (2012)) analysed in this work.

Gas	Line	Spectral	Start date	Duration	Sub-observer
	(μm)	resolution (μm)		(sec)	lat/lon
H ₂ O	66.43	0.0169	22/06/2010 23:49:52	3071	2.10°/283.74°
	75.38	0.039	22/06/2010 22:56:26	3079	2.10°/282.91°
	108.07	0.1127	22/06/2010 22:56:26	3079	2.10°/282.91°
CH ₄	106.43	0.1120	23/06/2010 00:43:14	1140	2.10°/284.59°
	119.63	0.1176	23/06/2010 00:43:14	1140	2.10°/284.59°

Table 3: *A priori* profiles considered for the H₂O retrieval (see also Figure 4).

Reference	Name	Type	Agreement	Comments
Moreno et al. (2012)	Sa	Measured	Herschel	Parametrized profile: $q = q_0 \times (p_0/p)^n$ with n the power law index
Dobrijevic et al. (2014)	IM1	Modelled	Herschel	Origin H ₂ O: micrometeorite ablation OH flux: $5.7 \times 10^5 \text{ cm}^{-2} \text{ s}^{-1}$
Dobrijevic et al. (2014)	IM2	Modelled	CIRS	Origin H ₂ O: micrometeorite ablation OH flux: $2.6 \times 10^6 \text{ cm}^{-2} \text{ s}^{-1}$
Dobrijevic et al. (2014)	IE1	Modelled	Herschel	Origin H ₂ O: Enceladus OH flux: $1.4 \times 10^6 \text{ cm}^{-2} \text{ s}^{-1}$
Lara et al. (2014)	L1	Modelled	Herschel	Time-dependent model, initial OH flux: $5.1 \times 10^6 \text{ cm}^{-2} \text{ s}^{-1}$ + loss to the haze
Lara et al. (2014)	L2	Modelled	CIRS	Time-dependent model, initial OH flux: $5.1 \times 10^6 \text{ cm}^{-2} \text{ s}^{-1}$ + loss to the haze
Lara et al. (2014)	L3	Modelled	CIRS	Time-dependent model, initial OH flux: 1.0 or $2.0 \times 10^7 \text{ cm}^{-2} \text{ s}^{-1}$

Table 4: Retrieved H₂O abundances and associated errors for the different observations analysed. The retrieved abundances are indicated for the two temperature profiles considered in this work. The given ranges describe the results arising from using the different *a priori* H₂O profiles listed in Table 3. Note that the pressure range is defined using the pressure levels at which the H₂O sensitivity is maximum (based on H₂O Jacobians). The total column of H₂O is calculated above the condensation level. For the comparison, the reported H₂O VMRs for the case using 1.00% of stratospheric CH₄ are given for the same pressure range.

Observation	H ₂ O VMR (ppb)	Total error	Pressure (mbar)	H ₂ O total column (molec/cm ²)	H ₂ O VMR (ppb) if 1.00% CH ₄	Previous retrieved H ₂ O
CIRS 182	0.120–0.215	-43%/+44%	8.2–5.1	$3.5\text{--}3.8 \times 10^{14}$	0.072–0.131	/
CIRS 202	0.080–0.151	-56%/+57%	8.2–5.1	$2.3\text{--}2.6 \times 10^{14}$	0.038–0.081	/
CIRS 206	0.059–0.119	-65%/+65%	8.0–5.1	$1.7\text{--}2.0 \times 10^{14}$	0.038–0.082	/
CIRS 219	0.054–0.120	-70%/+78%	8.2–4.7	$1.6\text{--}2.1 \times 10^{14}$	0.032–0.075	/
CIRS NA	0.058–0.109	-42%/+44%	9.6–5.4	$2.0\text{--}2.2 \times 10^{14}$	0.044–0.082	0.14±0.05 ppb at 10.7 mbar
PACS	0.024–0.052	-15%/+12%	8.2–5.6	$0.8\text{--}0.9 \times 10^{14}$	0.020–0.030	0.023±0.006 ppb at 12.1 mbar

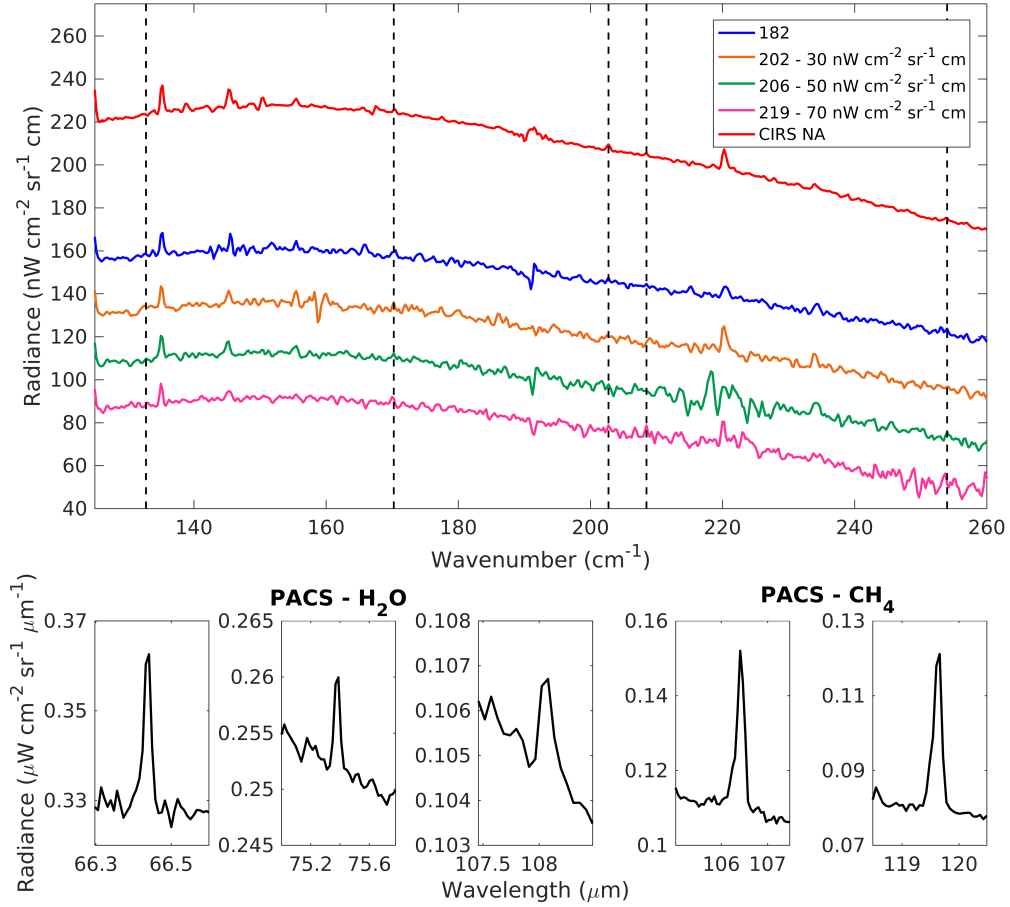


Figure 1: CIRS and PACS spectra analysed in this work. For display purposes, CIRS disc-averaged spectra have been offset vertically as indicated. H_2O lines, which are used for the retrieval, are identified for CIRS spectra with vertical dashed lines. PACS spectra are expressed in radiance units ($\mu\text{W cm}^{-2} \text{sr}^{-1} \mu\text{m}^{-1}$) as explained in the text.

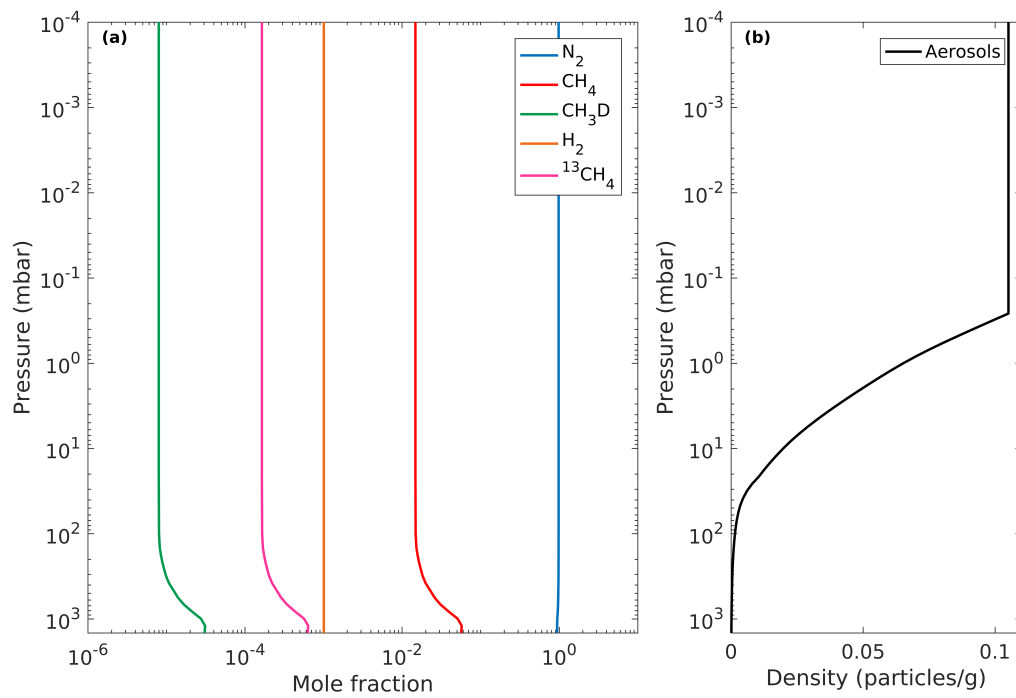


Figure 2: Main reference atmospheric vertical profiles used to simulate CIRS and PACS spectra: (a) Mole fraction of gases (Niemann et al., 2010), (b) Haze specific density (de Kok et al., 2007b, 2010b; Tomasko et al., 2008). See text for details.

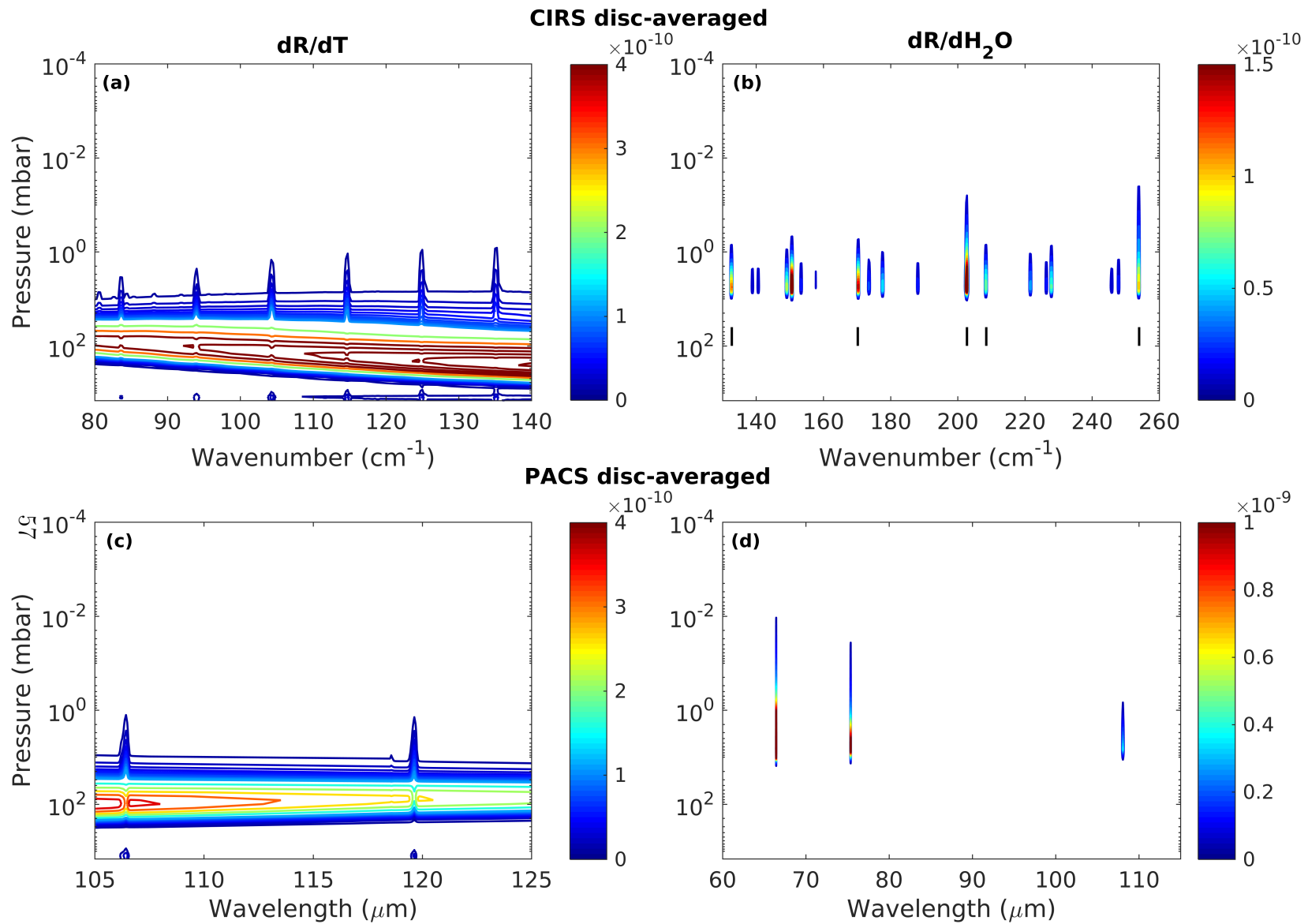


Figure 3: Jacobians of temperature and H₂O (color scales) calculated for disc-averaged observations of CIRS (a,b) and PACS (c,d). The Jacobians of H₂O are calculated for the “IM2” *a priori* profile (see Table 3 and Figure 4). For CIRS, the H₂O lines used in the retrieval are indicated with the vertical black lines.

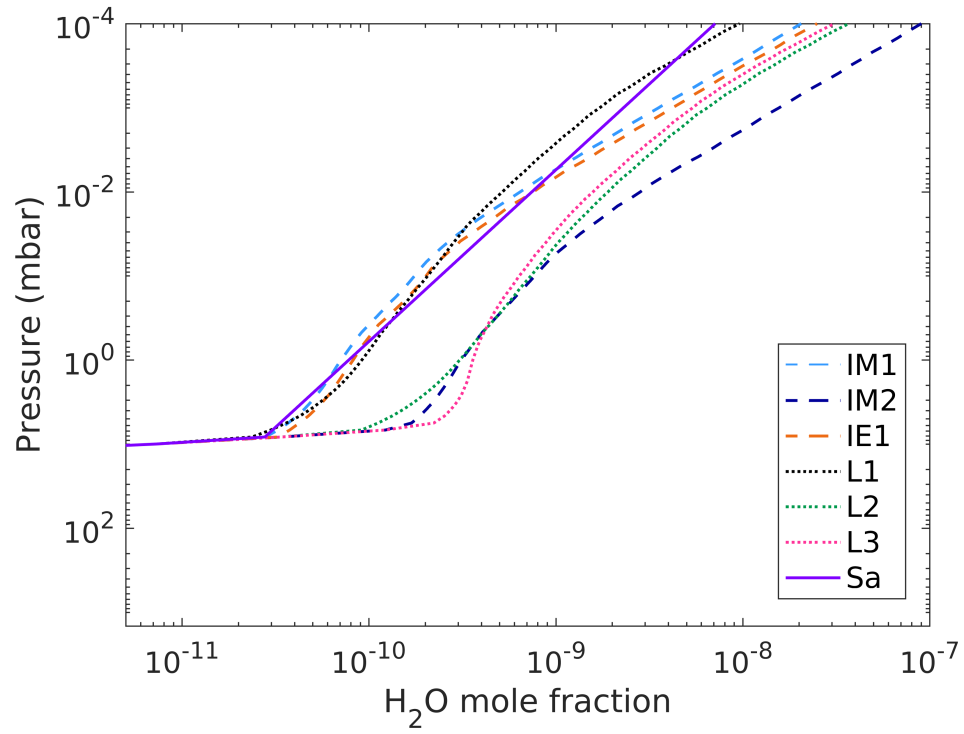


Figure 4: *A priori* profiles of H₂O considered in this work (see Table 3 for details).

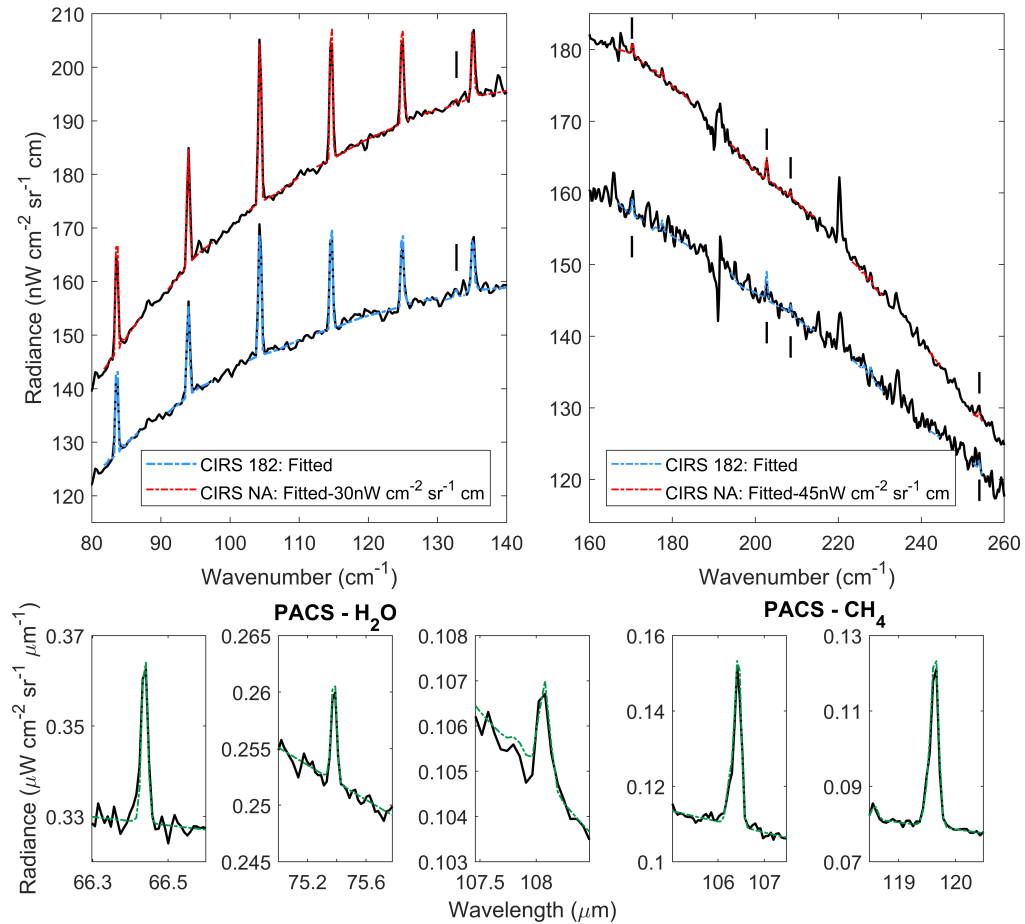


Figure 5: Example fits to the observed CIRS (set 182 and CIRS NA) and PACS spectra. For CIRS observations, they include the fits of the temperature retrieval, of the continuum and of the H₂O retrieval (considering the “IM2” *a priori* profile). Vertical lines indicate the fitted H₂O lines. For display purposes, the CIRS NA spectrum has been offset vertically as indicated. For PACS, the fits are shown for the H₂O and CH₄ lines analysed (considering the “Sa” *a priori* profile).

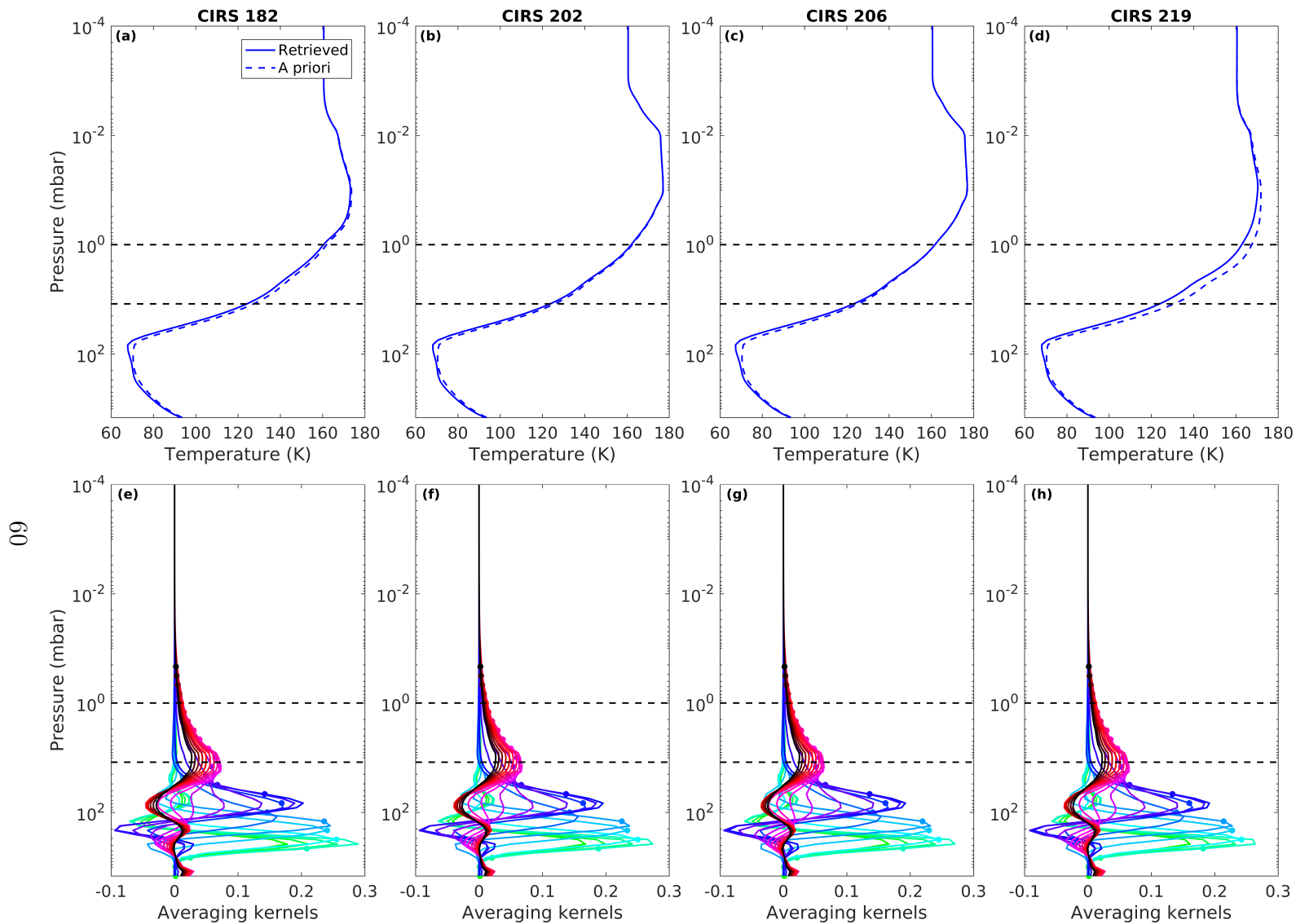


Figure 6: Retrieved and *a priori* temperature profiles (a-d) and associated averaging kernels functions (e-h) for the four sets of disc-averaged CIRS spectra. The black dashed lines delimit the region of maximum sensitivity to H₂O (12-1 mbar). For clarity, only one in every two averaging kernel functions until 0.2 mbar are shown. The dots indicate the pressure levels associated to each of these functions and a different colour is associated to each AVK function.

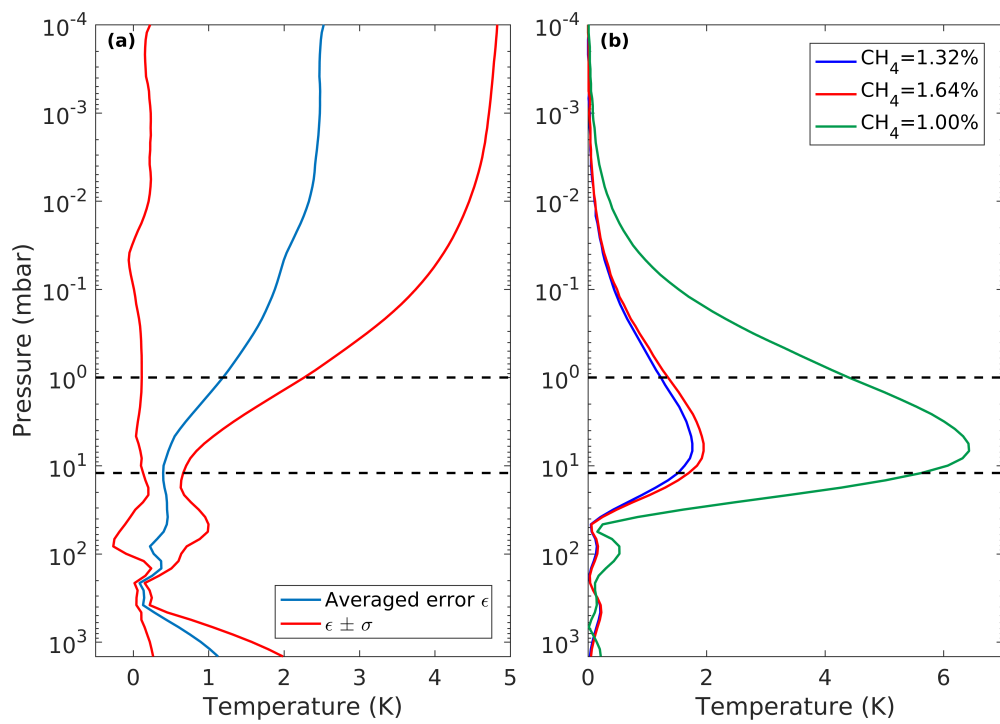


Figure 7: (a) Random error and its standard deviation calculated from retrievals on synthetic spectra. (b) Systematic errors (absolute values) on the retrieved temperature profile associated with the choice of CH_4 profile. The black dashed lines delimit the stratospheric region of sensitivity to H_2O abundance.

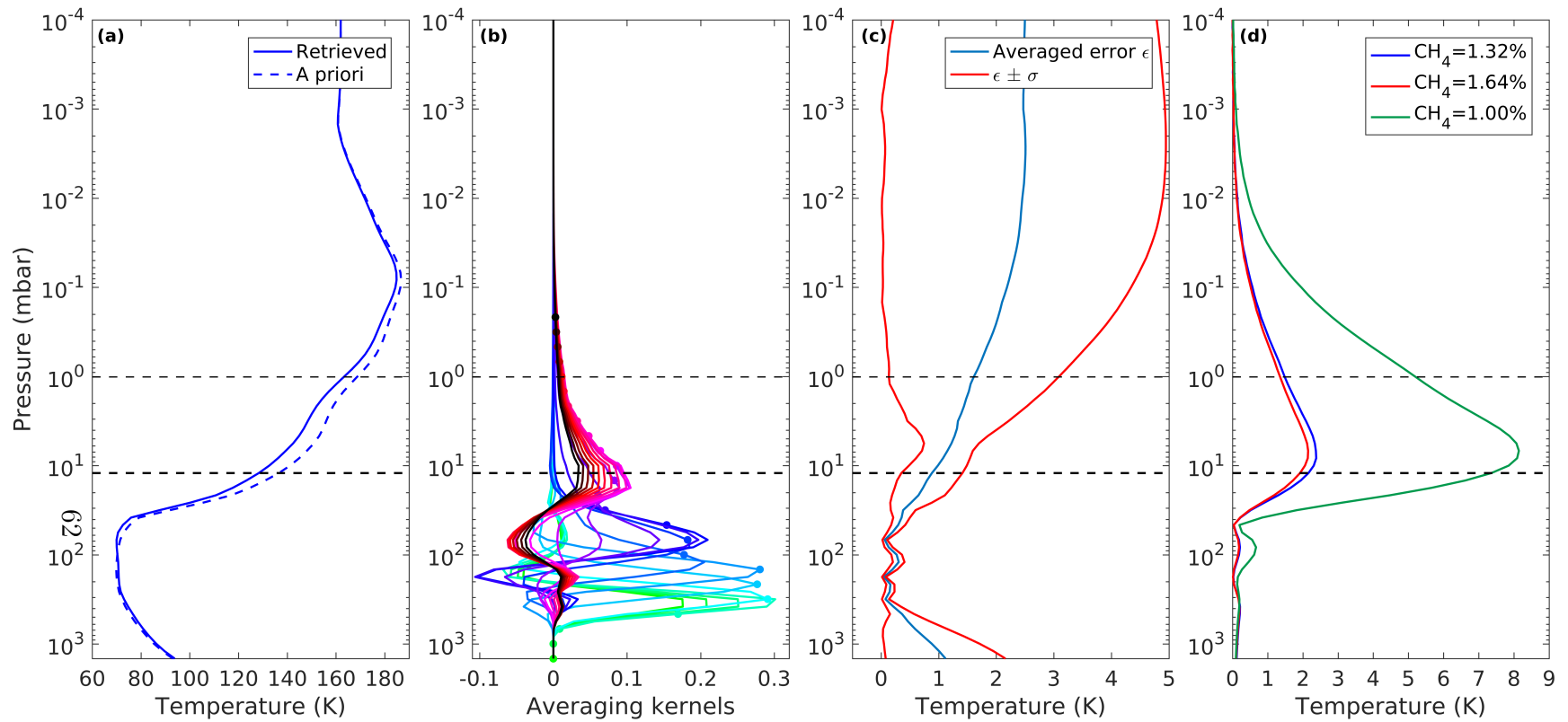


Figure 8: Temperature retrieval from the CIRS NA spectrum: (a) *A priori* and retrieved profile, (b) AVK functions associated to the retrieved profile, (c) Random errors and its standard deviation calculated from retrievals on synthetic spectra, and (d) Systematic errors (absolute values) on the retrieved temperature profile associated to the choice of CH_4 profile. The black dashed lines delimit the stratospheric region of sensitivity to H_2O abundance.

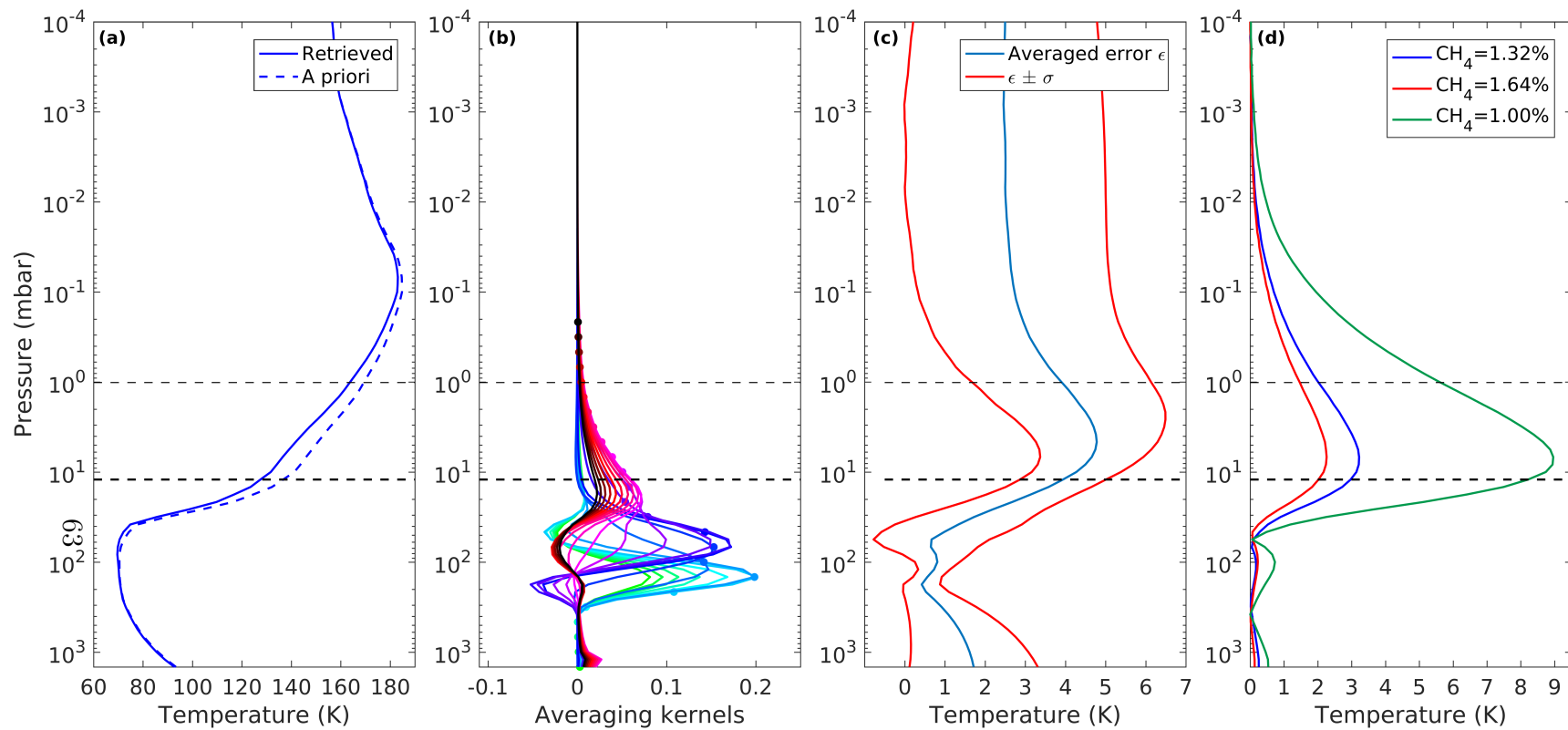


Figure 9: Same as Figure 8 but for PACS observations.

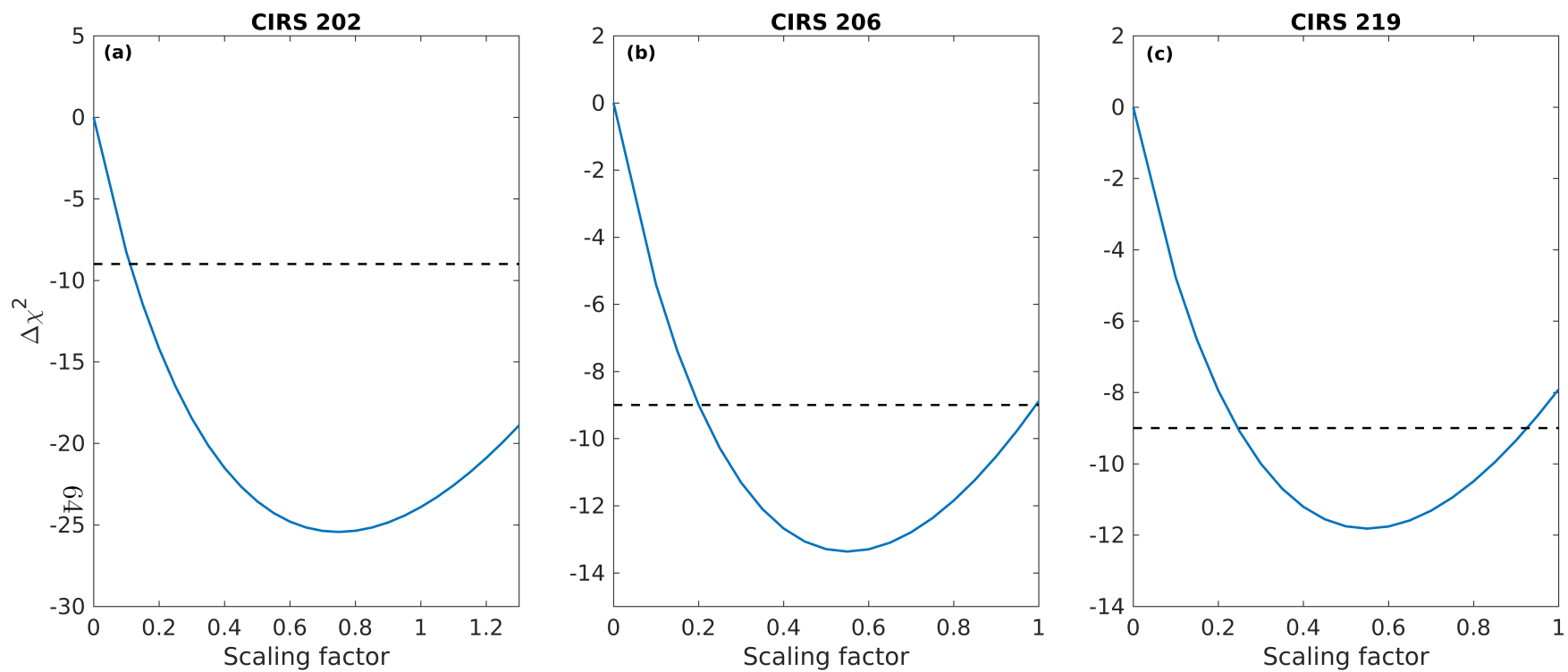


Figure 10: $\Delta\chi^2(\chi^2 - \chi^2(\text{MF} = 0))$ as a function of the scaling factor applied to the “IM2” H_2O *a priori* profile for the CIRS sets 202 (a), 206 (b), and 219 (c). The horizontal dashed line indicates the level of 3σ detection ($\Delta\chi^2 = -9$).

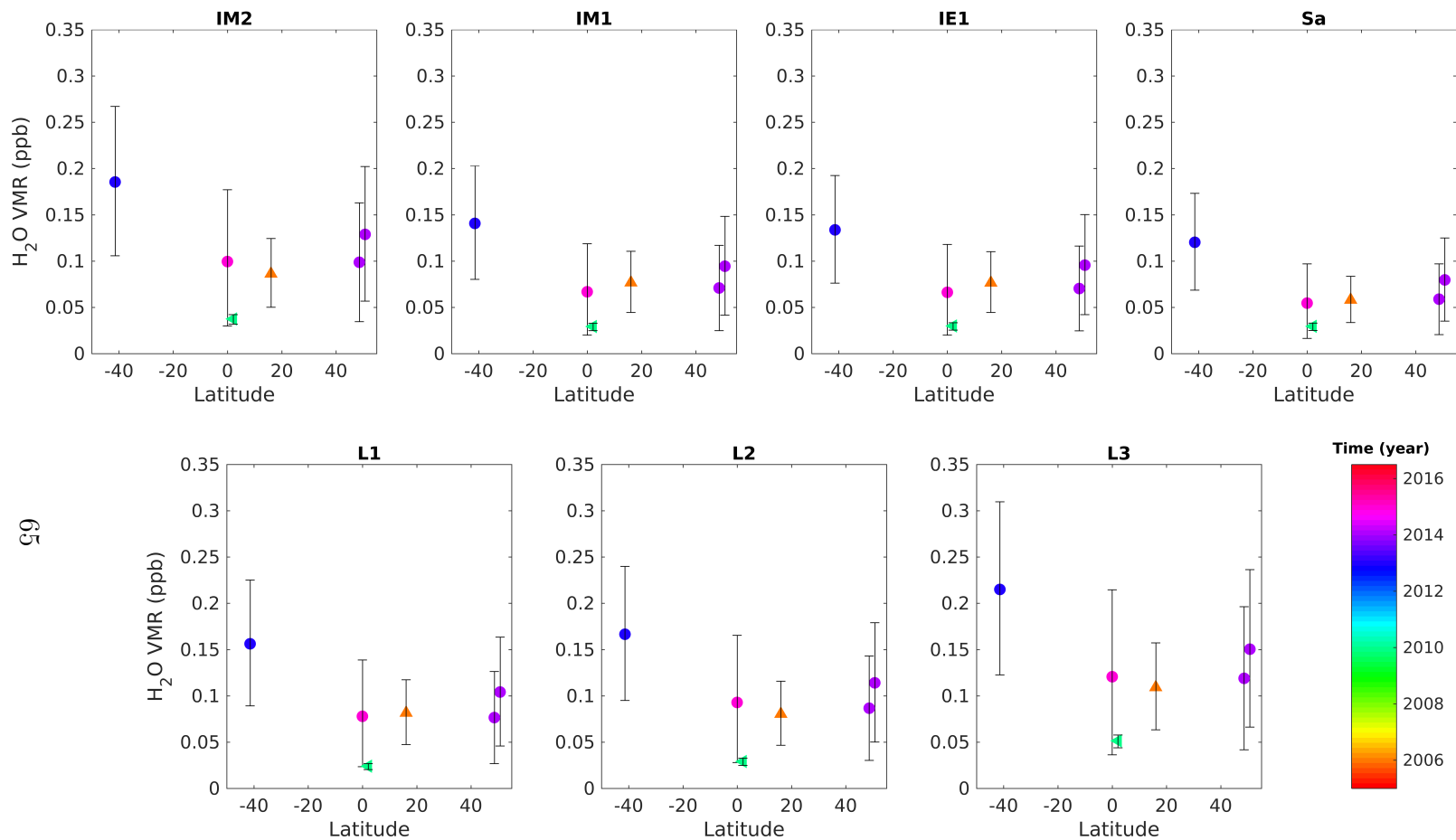


Figure 11: Retrieved H₂O VMRs for all observations as a function of latitude, of time (color scale) and of the *a priori* H₂O profile. These VMRs are retrieved using the stratospheric temperature profile determined using 1.48% for the stratospheric CH₄ mole fraction. The circles represent CIRS disc-averaged observations, the upward-pointing triangle the CIRS nadir observation, and the left-pointing triangle PACS observations.

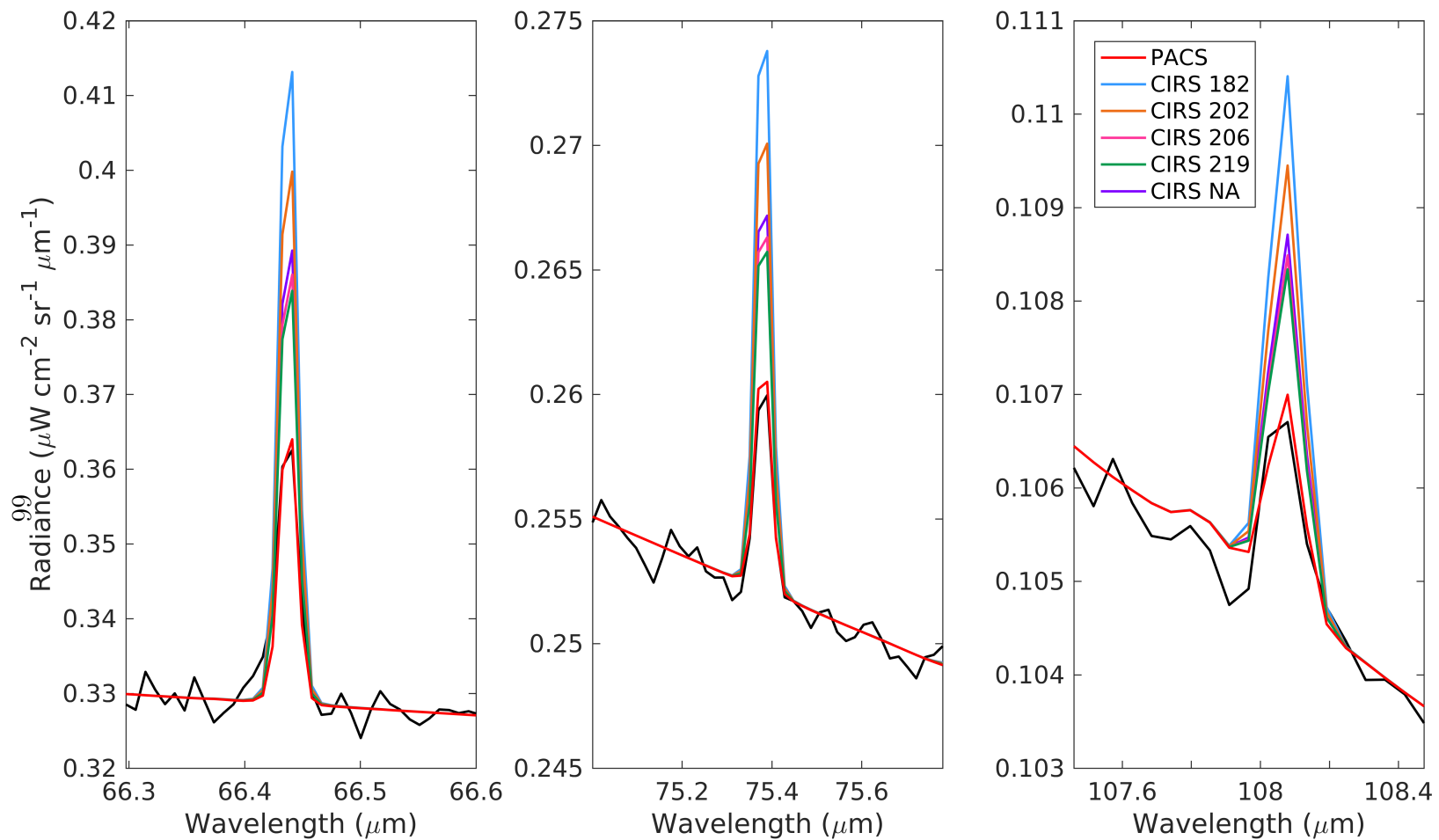


Figure 12: Comparison between observed PACS H₂O lines (black) and lines simulated using the H₂O profiles retrieved for the different observations (colored lines). The case using the “Sa” *a priori* profile has been considered (the profile has been scaled by the retrieved scaling factors) and using the stratospheric temperature profile determined using a stratospheric CH₄ mole fraction of 1.48%.